

Experimental Bedford limestone permeability dependence on confining stress and pore pressure. A comparative study with previous works

A. Domínguez-Torres¹, E. Serrano-Saldaña^{*1}, M. Coronado¹, M. A. Díaz-Viera¹ and I. Llanos-Rivera¹

Abstract

The impact of changes in the state of the confining stress and pore pressure on the permeability of a rock is especially important in the exploitation of oil reservoirs, particularly due to the decreases in the reservoir fluid pressure during the extraction of hydrocarbons. Over the years, numerous experimental studies have been conducted with core samples that have shown a wide range of responses. In the present study, this effect was analyzed in Bedford limestone. Two different modes of confinement, hydrostatic and non-hydrostatic, are investigated. The permeability data obtained from the experiments are fitted to commonly used models based on confining stress, core pressure and effective stress. The results indicate that the linear models offer a satisfactory fit in both confinement modes. A relatively high effective stress coefficient of 5.78 is observed in the hydrostatic mode, while an unusual negative value of -1.63 is found in the non-hydrostatic mode. These results were examined in the context of published permeability data and fitting models. To facilitate this analysis, complete tables were prepared that integrate the information available from the literature on permeability experiments in sandstones and limestones.

Key words: Permeability, confining stress, pore pressure, effective stress and effective stress coefficient.

Resumen

El impacto de los cambios en el estado del esfuerzo de confinamiento y de la presión de poro sobre la permeabilidad de una roca es muy importante en la explotación de yacimientos de petróleo, particularmente los cambios por la disminución de la presión del yacimiento durante la extracción de hidrocarburos. A lo largo de los años, se han realizado numerosos estudios experimentales con muestras de núcleos que han mostrado una amplia gama de respuestas. En el presente estudio, se analizó dicho efecto en una muestra de roca caliza Bedford. Se investigan dos modos diferentes de confinamiento, hidrostático y no hidrostático. Los datos de permeabilidad obtenidos de los experimentos se ajustan a modelos comúnmente utilizados basados en el esfuerzo de confinamiento, la presión de poro y el esfuerzo efectivo. Los resultados indican que los modelos lineales ofrecen un ajuste satisfactorio en ambos modos de confinamiento. Se observa un coeficiente efectivo de presión relativamente grande de 5.78 en el modo hidrostático, mientras que se encuentra un inusual valor negativo de -1.63 en el modo no hidrostático. Estos resultados se examinaron en el contexto de los datos de permeabilidad y modelos de ajuste publicados. Para facilitar este análisis, se elaboraron tablas completas que integran la información disponible de la literatura sobre experimentos de permeabilidad en areniscas y calizas.

Palabras clave: Permeabilidad, esfuerzo de confinamiento, presión de poro, esfuerzo efectivo y coeficiente efectivo de presión

Received: October 2, 2023; Accepted: March 26, 2024 Published on-line: July 1, 2024.

Editorial responsibility: Dr. Juan Pedro Morales Salazar

* Corresponding author: E. Serrano-Saldaña, eserrano@imp.mx

¹ Instituto Mexicano del Petróleo (IMP) Eje Central Lázaro Cárdenas Norte 152, San Bartolo Atepehuacán, Gustavo A. Madero, Ciudad de México.

Aarón Domínguez Torres, Enrique Serrano Saldaña, Manuel Coronado, Martín Alberto Díaz Viera, Iván Llanos Rivera

<https://doi.org/10.22201/igeof.2954436xe.2024.63.3.1742>

1. Introduction

The absolute permeability of a rock sample is a crucial petrophysical property that determines fluid flow capacity in a porous medium. It is influenced by various parameters, including fluid properties (density, viscosity, and chemical composition), fluid-rock interactions (mineral dissolution or precipitation), porous medium characteristics (mineralogy, clay content, compaction degree, geometry, pore distribution, fractures), and other factors related to the permeability measurement methodology (sample saturation, fluid injection rate, pressure, temperature) (Pål Ø, 2022). Additionally, the stress applied to the rock has also a significant impact on permeability (Glowacki & Selvadurai, 2016). In particular, the permeability dependence on applied stress is highly relevant in oil reservoirs since it profoundly impacts predictions of reservoir fluid flow behavior and influences the drilling and injection fluid design strategies during enhanced oil recovery.

The permeability dependence on confinement stress (σ_c) and the pore pressure (P_p) has been analyzed in terms of the so-called effective stress (σ'), defined as (Terzaghi, 1936)

$$\sigma' = \sigma_c - P_p \quad (1)$$

Later, Bernabé *et al.* (1986) introduced the effective stress coefficient (η_k), and Al-Wardy *et al.* (2004) showed its sensitivity to changes in σ_c and P_p .

The permeability dependence on effective stress

$$k = k(\sigma') \quad (2)$$

was explored, where

$$\sigma' = \sigma_c - \eta_k P_p \quad (3)$$

Numerous experimental studies have analyzed the permeability-stress dependency in water- or gas-saturated rock samples under different effective stress conditions. Response surface fitting methods and analytical models have shown that both sandstone and limestone samples exhibit permeability reductions, as effective stress increases as shown by Al-Wardy and Zimmerman (2004), Asaei (2013), Bernabé (1986), Berryman (1992), Da Silva, Schroeder and Verbrugge (2010), David *et*

al. (1994), Dong (2010), Ghabezloo *et al.* (2009), Glowacki and Selvadurai (2016), Li *et al.* (2009), Li *et al.* (2014), Meng *et al.* (2019), Nermoen *et al.* (2013), Nur *et al.* (1980), Qiao *et al.* (2012), Wang *et al.* (2018), Warspinski and Teufel (1992) and Zhao *et al.* (2011).

In this work, a series of experiments were conducted to identify and evaluate the effect of the stress state on the absolute permeability in water-saturated Bedford limestone samples. To this purpose, fluid displacement tests have been conducted using conventional equipment and methodologies at reservoir conditions (McPhee, Redd, & Zubizarreta, 2015).

Permeability measurements were performed under both confinement modes, with variations in pore pressure P_p ranging from 2 to 24 MPa and radial confinement stress σ_c between 3 and 27 MPa. The results show a significant permeability sensitivity to pore pressure. A constant value for the effective stress coefficient was calculated by linear regression analysis.

This work has six sections. The first section is an introduction that sets the context for the study. The second section presents the findings of a comprehensive literature review on the relationship between permeability and effective stress in sandstone and limestone samples. Section 3 provides detailed descriptions of the experimental procedure, including the equipment and fluid used and the methodology employed. Section 4 describes the experimental permeability results in hydrostatic and non-hydrostatic confinement mode. Section 5 presents an analysis and discussion of the experimental results, and the fitting models employed to describe the $k(P_p, \sigma_c)$ and $k(\sigma')$ behavior in both confinement modes. The experimental results are analyzed along with a comprehensive statistical study, encompassing correlation tests, experimental model fitting, and a comparison with results from previous studies. Lastly, Section 6 summarizes the main conclusions drawn from the research.

2. Literature Review

Table 1 and Table 2 present an analysis of reported experiments conducted on consolidated rocks to examine the influence of confinement stress, pore pressure, and effective stress on permeability. Table 1 focuses on sandstones, while Table 2 highlights findings on limestones. These tables provide a summary with authors, rock type, experimental conditions, and conclusions.

2.1. Sandstones

Table 1 shows various experimental studies on sandstones. The results indicate that permeability often exhibits a non-linear relationship with the effective stress σ' . The effective stress

coefficient is highly sensitive to changes in pore pressure and confinement stress; some η_k values are larger than unity and depends on the porosity, grain size and geometry. The experimental σ_c values fall between 0 and 45 MPa, except for the work by Zhao *et al.* (2011).

2.2. Limestones

Table 2 compiles published experimental works on limestones. Observations show that permeability is more sensitive to changes in pore pressure than changes in confinement stress. Frequently, the permeability follows an exponential decay in the confining stresses and the pore pressure. The η_k values are often lower than unity and depends on porosity, grain size,

microfractures presence, and microstructure. The permeability dependence on effective stress is often fitted by a polynomial function or in some cases by a power law (McPhee, Redd, & Zubizarreta, 2015; Selvadurai A. , 2021).

3. Experimental Procedure

3.1. Rock Sample

The samples are predominantly limestone. According to X-ray diffraction analysis, X-ray μ -CT and geomechanical characterization (Coronado, 2019), the Bedford limestone sample is 97% calcium carbonate, and 3% silicon oxide, with

Table 1. Published permeability experimental tests on sandstones.

Author	Rock type, conditions and methods	Conclusions
Dobrynin (1962)	Homogeneous quartz sample. Effective pressure from 0 to 138 MPa.	Porosity, density and permeability decrease with σ' , following a second-order polynomial.
Zoback & Byerlee (1975)	Berea sample. Confining stress range from 5 to 10 MPa and pore pressure constant at 2 MPa.	$k(\sigma')$ decreases linearly.
Nur <i>et al.</i> (1980)	Massillon sample. Confining stress range from 5 to 10 MPa and pore pressure constant at 2 MPa.	$k(\sigma')$ decreases linearly.
Bernabé, Y. (1986)	Chelmsford sample.	The effective stress coefficient (η_k) depends on the porosity, grain size and geometry. Fitting results of η_k (P_p , σ_c) are given.
Bernabé, Y. (1987)	Pottsville, Pigeon Cove and Westerly samples. Sensitivity analysis of η_k as function of σ' are performed.	η_k is highly sensitive to changes on P_p and σ_c .
David <i>et al.</i> (1994)	Berea and Boise samples. Pore pressure equals to 10 MPa and confining stress ranges from 3 to 13 MPa.	Porosity decreases following a power-law by increasing σ' , while k decreases exponentially by increasing σ' .
Al-Wardy & Zimmerman (2004)	Pore pressure ranges from 0 to 15 MPa and confining stress ranges from 5 to 20 MPa.	$k(\sigma')$ decreases linearly.
Li, M. B. <i>et al.</i> (2009)	Sandstones sample. Confining stress goes from 0 to 50 MPa and pore pressure from 0.2 to 0.8 MPa. Use of SRM (surface response method) to determine η_k .	η_k changes between 0 and 1, while $k(\sigma')$ decreases as a second order polynomial.
Zhao <i>et al.</i> (2011)	Heterogeneous sample. Confining stress ranges from 20 to 42 MPa and pore pressure goes from 0 to 30 MPa. The slide method is applied to evaluate η_k and determine the $k(\sigma')$ behavior.	$k(\sigma')$ decreases as a second order polynomial.
Qiao, L. P. <i>et al.</i> (2012)	A reservoir sample is used, with confining stress from 10 to 30 MPa and pore pressure from 0 to 25 MPa.	η_k values are larger than unity, due to the sample grain size.
Li M. X. <i>et al.</i> (2014)	Sandstones sample. Confining stress from 15 to 55 MPa and pore pressure from 5 to 25 MPa. Implementation of the secant method to determine η_k . Evaluation of the $k(\sigma')$ behavior.	η_k decays exponentially.
Choi <i>et al.</i> (2017)	Berea sample. Confining stress from 14 to 50 MPa and pore pressure from 10 to 23 MPa. Evaluation of $k(\sigma')$ in a process of CO ₂ injection.	η_k increases non-linearly in the confining stress from 38 to 42 MPa and pore pressure from 8 to 20 MPa. $k(\sigma')$. It follows a power law model.
Nolte <i>et al.</i> (2021)	Tight sandstone sample. Evaluation $k(\sigma')$ by gas injection. Here confining stress ranges from 10.3 MPa to 49 MPa and pore pressure from 0.3 to 30 MPa.	An effective stress coefficient of 1.25 and a volumetric deformation coefficient of 0.7 were found.

13% average effective porosity, and throat pore size between 40 to 52 μm . Representative images of the rock sample and its pore structure are shown in Figure 1 and Figure 2 respectively. Their main physical and mechanical properties are described in Table 3.

3.2. Fluids

Distilled water was used in the experiments as displacing fluid. By this way, pore damage and pore obstruction by mineral deposition and scale formation that could appear by rock-water incompatibility is avoided. These processes would alter permeability measurements. Additionally, the alkaline nature of double distilled (pH=9.34 at 295°K) minimizes calcite dissolution (Lisabeth & Zhu, 2015).

3.3. Equipment

The standard configuration of a Hassler coreholder lacks confinement stress control, therefore, resulting in a non-hydrostatic confinement condition, where the radial confinement stress differs from the axial stress. To establish hydrostatic confining stress

conditions, modifications were made to the standard Hassler coreholder configuration.

The general configuration of the experimental equipment is shown in Figure 3. Hassler coreholder is conventionally used in SCAL tests (McPhee, Redd, & Zubizarreta, 2015), and can only work in non-hydrostatic confinement mode, where the radial stress is indeed controlled, but not the axial stress, since axial plates are fixed. In this research however, Hassler coreholder modifications were made to run $k(\sigma')$ experiments in both hydrostatic and non-hydrostatic confinement mode. Figure 4a illustrates the coreholder adaptations to reach the hydrostatic conditions, while Figure 4b shows the original configuration used to get the non-hydrostatic conditions. In the non-hydrostatic confinement mode, the radial stress is established by injecting the confinement fluid inside the free space between the coreholder and the core sample, by this way, the radial stress is directly controlled by the Quizix pump.

3.4. Procedure

The experiments were conducted under the following conditions:

Table 2. Published experimental studies on limestones.

Author	Rock type, conditions and methods	Conclusions
Selvadurai & Glowacki. (2008)	Indiana sample. Confining stress ranges from 5 to 60 MPa and pore pressure from 5 to 25 MPa.	$k(\sigma_c)$ shows an exponential decay of 14% by increasing effective pressure from 0 to 60 MPa.
Ghabezloo et al. (2009)	Homogenous oolite. Confining stress from 3 to 12 MPa and pore pressure from 1.05 to 3.05 MPa.	$\eta_k(P_p, \sigma_c)$ displays a linear dependence with P_p and σ_c . $k(\sigma')$ is fitted by a power law.
Da Silva et al. (2010)	Isotropic calcite. Measurement of $k(\sigma')$ in a drained and undrained mode at confining stress from 5.5 to 35.5 MPa and pore pressure equals to 5 MPa.	$\eta_k(\sigma')$ behaves non-linearly in both modes.
Glowacki & Selvadurai. (2016)	Indiana sample. Confining stress from 2 to 9 MPa and pore pressure from 0 to 30 MPa.	The permeability decreases up to 80% failure load.
Selvadurai & Glowacki (2017)	Ordovician sample. Tests in the effective pressure range from 5 to 30 MPa.	$k(\sigma')$ decreases exponentially.
Wang et al. (2018)	Indiana, Leitha, Thala and Purbeck samples. Tests in the confining stress range from 3.8 to 16.4 MPa and pore pressure from 1.2 to 5.7 MPa.	The η_k values change from 0.3 to 5. $k(\sigma')$ shows an exponential behavior.
Meng et al. (2019)	Indiana and Purbeck samples. Pore pressure equals 5 MPa and confining stress ranges from 10 to 55 MPa.	$k(\sigma')$ displays an exponential behavior and $\phi(\sigma')$ follows a power law dependence.
Selvadurai (2021)	Consolidated soil. The irreversibility of structure deformations is examined.	Consolidation Terzaghi's theory is used.
Bohnsack et al. (2021)	Carbonate rock samples. The permeability and porosity as a function of the effective stress is evaluated. Effective pressure in the range of 0 to 28 MPa.	0.7% to 2.1% porosity reduction by effective stress increase, while permeability corresponds decreases between 17.3% and 56.7%.

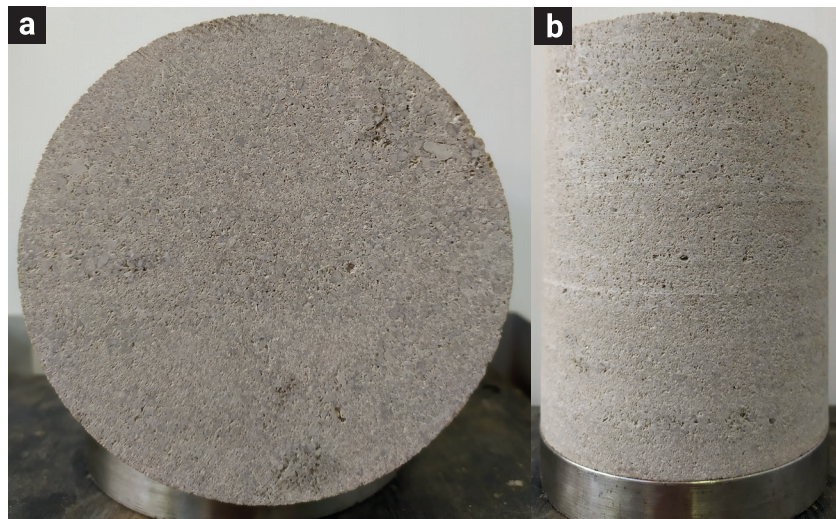


Figure 1. Bedford limestone samples used in this work.

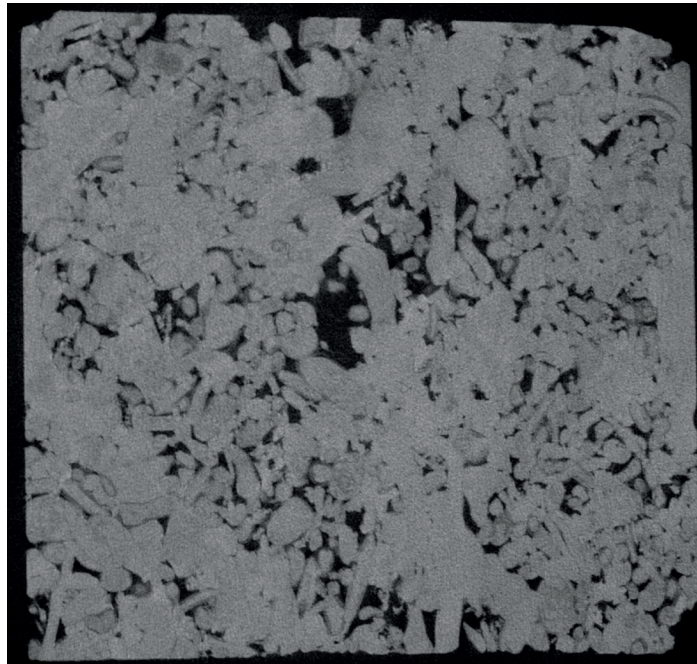


Figure 2. μ CT image of a $1\text{cm} \times 1\text{cm}$ section of the Bedford limestone used in this work.

1. Confining stress:

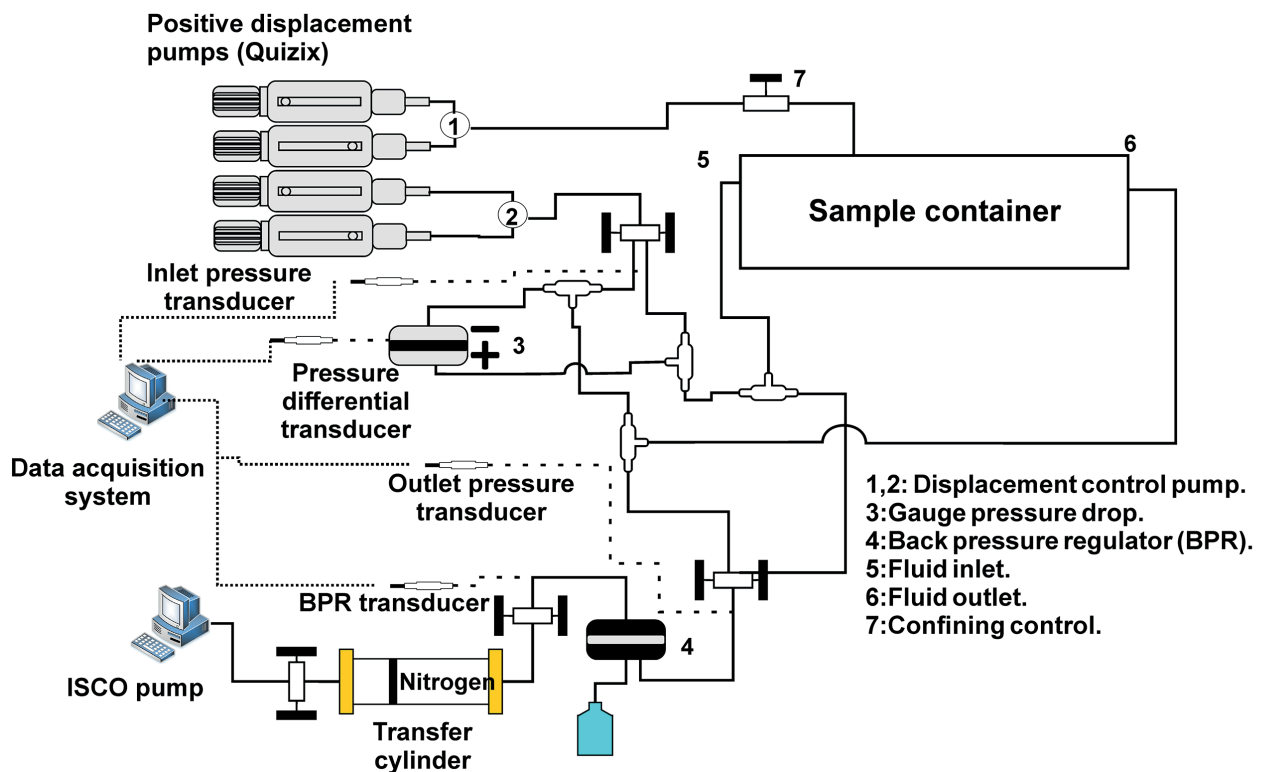
- a. Confinement system operates in non-hydrostatic mode when the radial confinement stress differs from the axial stress, as illustrated in Figure 5a. In this case, steel spacers and diffusers are attached to the coreholder cap, and maintain the core sample axial faces fixed, without any displacement.
- a. The confinement system operates in hydrostatic mode when axial stress equals the confinement stress in radial

direction as illustrated in Figure 5b. In this case, no steel spacers are used, and diffusers and rock are embedded in the confining fluid.

2. The pore pressure, P_p , is taken as the direct average value of the inlet pressure (P_{in}), and the outlet pressure (P_{out}). The fluid is injected and pressurized into the rock by the Quizix pump, so the flow rate is adjusted to set the desired inlet pressure. The outlet pressure is controlled and set by an ISCO pump on the back pressure regulator (BPR).

Table 3. Physical and mechanical properties of the sample.

Properties	Units	Sample A	Sample B
Core length (L)	m	0.1230	0.1270
Core diameter (D)	m	0.1020	0.1016
Core cross-sectional area (A)	m^2	8.171×10^{-3}	8.107×10^{-3}
Rock volume (V_r)	m^3	1.000×10^{-3}	1.030×10^{-3}
Core dry weight (W_d)	kg	2.18	2.25
Grain density	kg/m^3	2711	2711
Porosity (ϕ)	%	14.02	13.63
Reference permeability (k_{ref})	m^2	1.083×10^{-13}	1.491×10^{-13}
Young's modulus (E)	GPa	27.6	27.6
Poisson's ratio		0.19	0.19
Biot coefficient	-	0.78	0.78

**Figure 3.** Displacement system configuration.

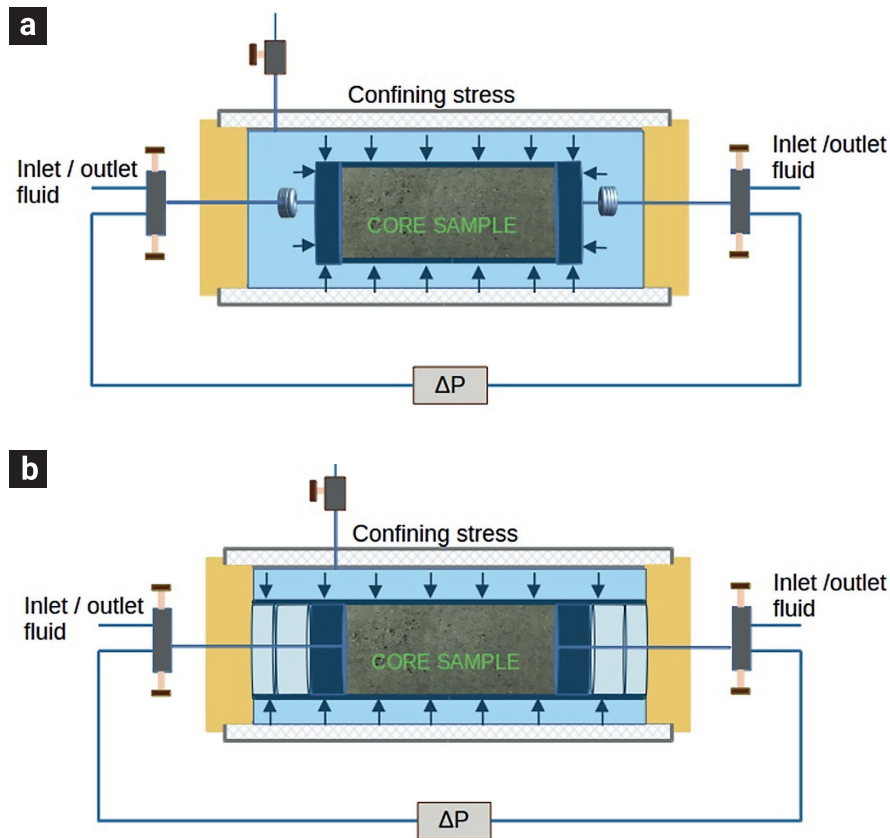


Figure 4. Coreholder used for a) hydrostatic confinement mode configuration, and b) non-hydrostatic confinement stress mode.

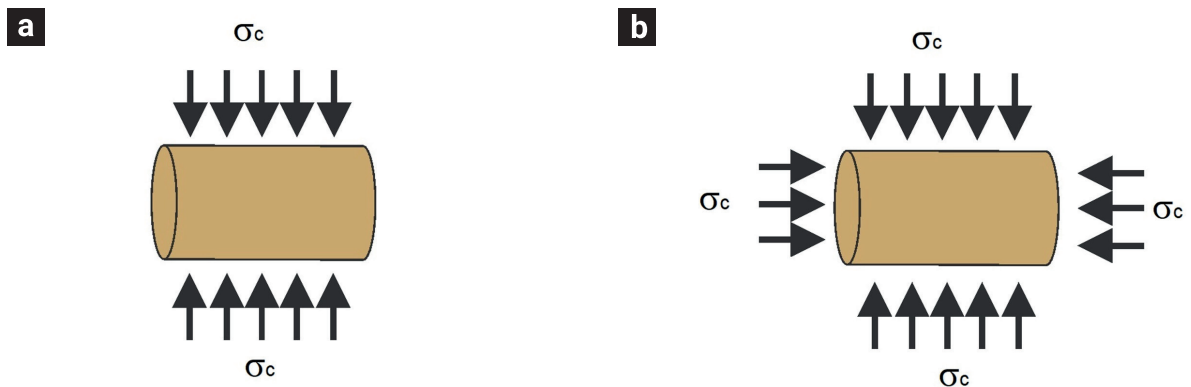


Figure 5. Confining stress modes: a) Non-hydrostatic and b) Hydrostatic.

3. Rock stress state is given by P_p and σ_c at each experiment.
4. In all cases, samples are 100% water saturated at a reference pressure of 6.89 MPa.
5. Loading and unloading cycles were applied to minimize memory effects in the rock.
6. To prevent sleeve rupture, a constant minimum pressure difference ($\sigma_c - P_p$) was maintained as low as 4.13 MPa.

3.4.1. Sample Characterization

A clean dry rock sample in a rubber sleeve is placed in the coreholder and the displacement system assembled. Vacuum is set for a period of 2 hours to avoid air presence. Distilled water was injected at room temperature until the inlet pressure reaches a plateau after 48 h at 6.89 MPa. Permeability tests were per-

formed on samples A and B at four constant flow rates 1, 2, 3, and 4 *ml/hr*. Pressure drop was measured for approximately 30 min and the average value was taken to evaluate the permeability by Darcy's law.

$$k = \frac{QL\mu}{A\Delta P} \quad (4)$$

Here Q is the flow rate, A is the core section area, ΔP is the pressure drop along the sample, L is the core length and μ is the fluid dynamic viscosity. The laminar flow assumption behind Darcy's law (Glowacki & Selvadurai, 2016) and (Selvadurai & Selvadurai, 2010) is satisfied, since the estimated pore fluid velocity is $5.0 \times 10^{-5} \text{ m/s}$. This corresponds to a small Reynolds number (R_e) of 0.003, that satisfies the Philips (1991) condition $R_e < \phi$, and Bear (1972) condition $R_e < 0.1$ for laminar flow in a porous media.

3.4.2. Hysteresis Effect Reduction

In order to reduce hysteresis effects, the rock sample preparation follows recommendations described by Asaei & Moosavi (2013), Bernabé (1986), Bernabé (1987), Bernabé (1988) and Hart & Wang (1995). The rock sample is set to at least two cycles of loading-unloading, increasing σ_c from 2.75 to 27.57 *MPa* in steps of 0.68 *MPa*, while keeping P_p constant at 2.06 *MPa*. Once the highest-pressure value is achieved, pressure is decreased at constant rate until the cycle is complete. At the end of the cycle, a rest period of approximately 0.45 hours is set. According to Warspinski and Teufel (1992), hysteresis effects become negligible after a few conditioning cycles.

3.4.3. Permeability Evaluation Method

The permeability of the rock sample was estimated by employing the pressure drop recorded data at each step and using Darcy's law Eq. (4). The layout experimental conditions are shown in Table 4. Water injection is controlled by the pump at constant pressure mode, while the confining stress is set by the Quizix pump. The outlet pressure is controlled by the ISCO pump at constant pressure, working through the BPR. The experiments were performed starting with the lowest P_p and σ_c values in the series displayed in Table 4. To avoid nonlinear rock sample responses, confining stress was kept below 28 *MPa*. After a pressure stabilization period, the permeability is evaluated. Further, σ_c is increased to its next value, while keeping the same P_p value. After the required stabilization period, a new permeability value is evaluated. This process is repeated until the entire series of P_p and σ_c is completed.

The recorded parameters are time, injection rate, total liquid injected volume, injection pressure, outlet pressure, BPR pressure and pressure drop. The measurement time in each experiment is long enough to get sufficient data for statistical analysis.

4. Experimental Results

Permeability results are presented in Table 5 and Table 6 for the hydrostatic and non-hydrostatic confinement mode, respectively, and graphically shown in Figure 6 to Figure 9. The data has been statistically analyzed, and the results are visually depicted in box plots displayed in Appendix A. Furthermore, the experimental results obtained from both the hydrostatic and non-hydrostatic modes have been employed by Vadillo-Sáenz *et*

Table 4. Experimental conditions to evaluate the stress state effect on the absolute permeability in limestone rock samples.

Sample	Compression mode	Number of experiments	Pore pressure (MPa)	Confining stress (MPa)
Limestone A	Hydrostatic	8	2.06, 4.13, 6.20, 8.27, 10.34, 13.79, 17.24, 20.68.	3.45, 6.89, 10.34, 13.79, 20.68, 27.58
Limestone B	Non-hydrostatic	6	6.89, 10.23, 13.78, 17.23, 20.68, 24.13.	9.65, 11.03, 12.41, 13.78, 19.30, 22.06, 24.82, 27.57.

Table 5. Median permeability as a function of confining stress and pore pressure in the hydrostatic mode in Sample A.

σ_c (MPa)	P_p (MPa)							
	2.07	4.14	6.21	8.27	10.34	13.79	17.24	20.68
3.45	Permeability ($\times 10^{-13}$)(m^2)							
6.89	1.08							
10.34	1.09	1.16	1.17					
13.79	1.08	1.17	1.16	1.15				
20.68	1.08	1.15	1.15	1.16	1.18			
27.58	1.07	1.15	1.15	1.15	1.17	1.21	1.22	
	1.06	1.13	1.13	1.14	1.16	1.20	1.20	1.21

Table 6. Median permeability as a function confining stress and pore pressure in the non-hydrostatic mode in Sample B.

σ_c (MPa)	P_p (MPa)					
	6.89	10.34	13.78	17.23	20.68	24.13
11.03	Permeability ($\times 10^{-13}$)(m^2)					
12.41	1.39					
13.78	1.38	1.29				
19.30	1.38	1.30				
22.06	1.33	1.29	1.13	1.15		
24.82	1.34	1.26	1.10	1.13	1.17	
27.57	1.30	1.26	1.04	1.13	1.18	1.10
	1.27	1.23	1.07	1.13	1.10	1.10

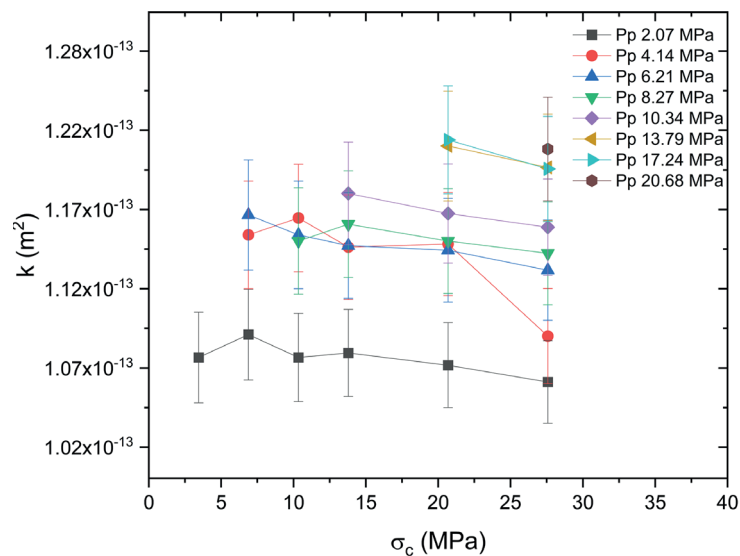


Figure 6. Permeability in hydrostatic confinement mode as function of the confining stress at various constant pore pressure.

al. (2022), to fit a poroelastic model that describes the permeability behavior as function of pore pressure and confinement stress in a Bedford limestone. The porosity dependence on confining stress was not measured since strain gauges to measure the axial or volumetric core deformation were not available.

4.1. The Hydrostatic confinement mode

Median values of the permeability in the hydrostatic confinement mode are presented in Table 5 and graphically displayed in Figure 6 and Figure 7. Figure 6 shows k as a function of σ_c for different values of P_p . Figure 7 shows k as a function of P_p for different σ_c values. The permeability error bar in the plots has been evaluated according to Appendix B. Figure 6 and Figure 7 the expected general behavior trend is found (within the error bars), i.e., permeability decreases by increasing the confining stress at constant pore pressure, and permeability increases by increasing the pore pressure at constant confining stress.

4.2. The non-hydrostatic confinement mode

Median permeability values in the non-hydrostatic confinement mode are presented in Table 6. Figure 8 shows k as a function of σ_c for different values P_p . The expected general trend is seen, i.e., the permeability reduces by increasing σ_c . A strange behavior (outside the range of error bars) is that the curve associated with $P_p=13.78$ MPa (depicted by blue triangles) appears systematically below to all other curves, whereas one would expect it to be above the $P_p=17.23$ MPa curve. This unexpected

result suggests a potential alteration in the experimental conditions. Additionally, it is worth noting that the final data point of the $P_p=20.68$ MPa curve (violet diamonds) falls below the $P_p=17.32$ MPa curve. In Figure 9 the permeability as function of P_p is displayed. The general trend shows a different behavior from what would be expected, since permeability reduces with increasing pore pressure. At the central plot region, around $P_p=13.78$ MPa, the curves show an out-of-trend fall. This fall has the same origin mentioned previously in Figure 8, regarding the $P_p=13.78$ MPa data series, and it is possibly caused by an experimental out of control condition.

5. Analysis and Discussion

It is important to highlight that commonly reported data fitting techniques often involve lumping permeability data into separate series of equal confinement stress value, and then fitting each data series separately. This procedure leads to an effective stress coefficient, η_k , that varies with the confinement stress, σ_c . However, this approach contradicts the fundamental concept of the effective stress coefficient, this is, that η_k is a constant that captures the overall stress response of the rock through a single variable, which is the effective stress, σ' . The fitting procedure followed in this work considers the whole data set at once, giving place to an indeed constant η_k value. Being η_k a constant, the effective stress fully encompasses the combined influence of both pore pressure (P_p) and confinement stress (σ_c), ensuring a comprehensive representation of the rock behavior.

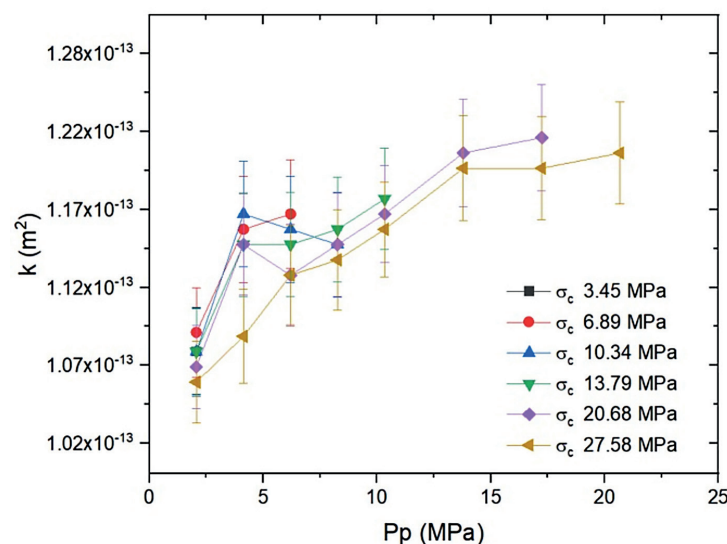


Figure 7. Permeability in the hydrostatic confinement mode as function pore pressure at various constant confining stresses.

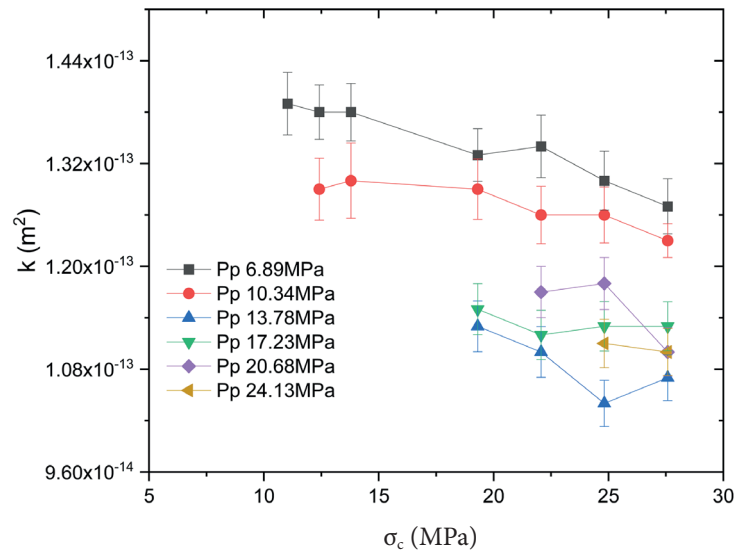


Figure 8. Permeability in the non-hydrostatic confinement mode as function of stress at various constant pore pressures.

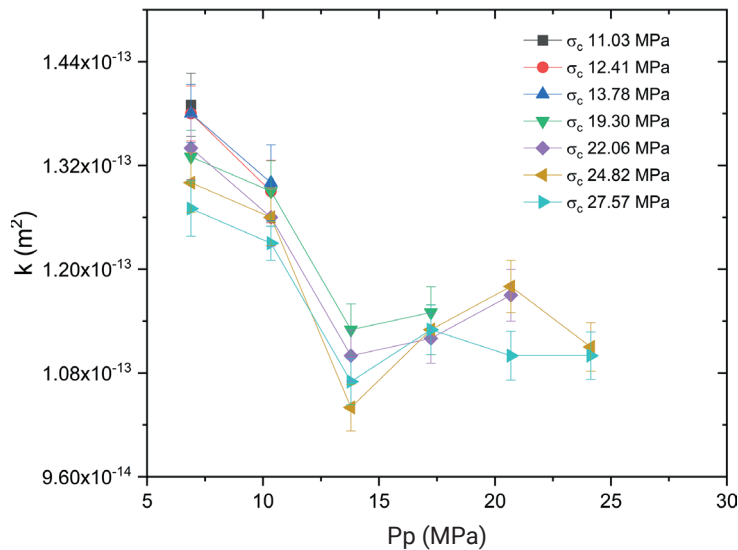


Figure 9. Permeability in the non-hydrostatic confinement mode as function of pore pressure at various confining stresses.

5.1. Correlation Analysis

A bivariate statistical analysis has been performed to determine possible correlations between permeability, pore pressure and confining stress, in both confinement modes. The Spearman correlation method was employed, which allowed nonlinear monotonic relationships. A Spearman correlation coefficient of 1 or -1 means that permeability follows a perfect monotonic dependence on P_p or σ_c . The Spearman coefficient obtained for permeability in the hydrostatic confinement mode is 0.86 on pore

pressure and 0.12 on confinement stress. On the other side, for the non-hydrostatic mode, the obtained Spearman coefficients are -0.81 and -0.63 respectively. In both cases a stronger permeability correlation on pore pressure than to confinement stress is found. The results indicate that in the hydrostatic mode, k is more sensitive to changes in P_p than to changes in σ_c . In the non-hydrostatic mode, permeability is equally sensitive to changes in P_p as to changes in σ_c . In the hydrostatic mode k increases with P_p and reduces with σ_c , while in the non-hydrostatic mode, k reduces with both P_p and σ_c .

5.2. Fitting Models

In this section, the permeability dependence on confining stress and pore pressure is analyzed in terms of various algebraic models traditionally used in the literature. Permeability data are commonly analyzed with a primary focus on effective stress. Various functionalities, such as power law Ghabezloo *et al.* (2009), exponential David *et al.* (1994) and Wang *et al.* (2018) or polynomial Zhao *et al.* (2011) are explored. In this work, permeability model fitting is first examined in terms of both variables, σ_c and P_p , and later, in terms of the effective stress, σ' .

5.2.1. Permeability data fitting in terms of P_p and σ_c

In the literature, permeability as a function of pore pressure and confining stress has been fitted by diverse models. One of them is the quadratic model Han *et al.* (2022), Li *et al.* (2009), Li *et al.* (2014) and Wang *et al.* (2018) with six fitting parameters (from A_0 to A_5)

$$k = A_0 + A_1\sigma_c + A_2P_p + A_3\sigma_cP_p + A_4\sigma_c^2 + A_5P_p^2 \quad (5)$$

Other models employed are a linear model with crossover dependence Choi *et al.* (2017) and Han *et al.* (2022), which have four fitting parameters,

$$k = A_0 + A_1\sigma_c + A_2P_p + A_3\sigma_cP_p \quad (6)$$

A linear model with three fitting parameters

$$k = A_0 + A_1\sigma_c + A_2P_p \quad (7)$$

And an exponential decay model with 3 fitting parameters

$$k = A_0e^{A_1\sigma_c + A_2P_p} \quad (8)$$

At low σ_c and P_p values the exponential model reproduces the linear model behavior. In this work, the least squares method (LSM) is used to fit hydrostatic and non-hydrostatic permeability data to each of these four previous models. In fitting the exponential model, the natural logarithm of Eq. (8) is taken, thus a linear expression follows, $\log k = \log A_0 + A_1\sigma_c + A_2P_p$, and the LSM can be applied.

Model fitting results for the hydrostatic and non-hydrostatic confinement mode are presented in Table 7 and Table 8, respectively. RMSE is a standard measure to evaluate the error in fitting procedures, whereas R^2 provides a measure of the model fitting goodness. The results of the hydrostatic confinement mode show that the best fitting models (the smallest RMSE combined with the largest R^2 value) in decreasing order are quadratic model (6 fitting parameters), linear with crossing model (4 parameters), linear model (3 parameters) and exponential model (3 parameters). Choosing a specific model depends on the objectives of the study and the desired stress range. To maintain simplicity, researchers often opt for a model with a less complex algebraic structure and minimal number of fitting parameters. Thus, in hydrostatic mode, the linear model is recommended.

Similar conclusions follow from Table 8 regarding the non-hydrostatic confinement mode. In Figure 10 and Figure 11 the permeability data points, and the fitting linear model

Table 7. Fitting model parameter values for hydrostatic confinement mode (Sample A).

Parameters	Linear	Linear with Crossing	Quadratic	Exponential
A_0	$1.108 \times 10^{-13} m^2$	$1.073 \times 10^{-13} m^2$	$1.061 \times 10^{-13} m^2$	$1.109 \times 10^{-13} m^2$
A_1	$-1.497 \times 10^{-16} m^2 MPa^{-1}$	$1.517 \times 10^{-16} m^2 MPa^{-1}$	$1.574 \times 10^{-16} m^2 MPa^{-1}$	$-1.326 \times 10^{-16} m^2 MPa^{-1}$
A_2	$8.653 \times 10^{-16} m^2 MPa^{-1}$	$1.566 \times 10^{-16} m^2 MPa^{-1}$	$1.627 \times 10^{-16} m^2 MPa^{-1}$	$7.561 \times 10^{-16} m^2 MPa^{-1}$
A_3		$-3.041 \times 10^{-16} m^2 MPa^{-1}$	$9.673 \times 10^{-16} m^2 MPa^{-2}$	
A_4			$-1.030 \times 10^{-16} m^2 MPa^{-2}$	
A_5			$-4.966 \times 10^{-16} m^2 MPa^{-2}$	
RMSE	$2.245 \times 10^{-15} m^2$	$2.071 \times 10^{-15} m^2$	$1.787 \times 10^{-15} m^2$	$2.202 \times 10^{-15} m^2$
R^2	0.7560	0.7923	0.8453	0.7438

Table 8. Fitting model parameter values in the non-hydrostatic confinement mode (Sample B).

Parameters	Linear	Linear with Crossing	Quadratic	Exponential
A_0	$1.159 \times 10^{-13} m^2$	$1.747 \times 10^{-13} m^2$	$1.760 \times 10^{-13} m^2$	$1.574 \times 10^{-13} m^2$
A_1	$-7.294 \times 10^{-16} m^2 MPa^{-1}$	$-1.649 \times 10^{-16} m^2 MPa^{-1}$	$-6.423 \times 10^{-16} m^2 MPa^{-1}$	$-5.840 \times 10^{-16} MPa^{-1}$
A_2	$-1.186 \times 10^{-13} m^2 MPa^{-1}$	$-3.473 \times 10^{-16} m^2 MPa^{-1}$	$-5.127 \times 10^{-16} m^2 MPa^{-1}$	$-9.738 \times 10^{-16} m^2 MPa^{-1}$
A_3		$9.439 \times 10^{-16} m^2 MPa^{-2}$	$-1.164 \times 10^{-16} m^2 MPa^{-2}$	
A_4			$2.157 \times 10^{-16} m^2 MPa^{-2}$	
A_5			$1.440 \times 10^{-16} m^2 MPa^{-2}$	
RMSE	$5.870 \times 10^{-15} m^2$	$5.638 \times 10^{-15} m^2$	$4.497 \times 10^{-15} m^2$	$5.302 \times 10^{-15} m^2$
R²	0.7047	0.7275	0.8267	0.6888

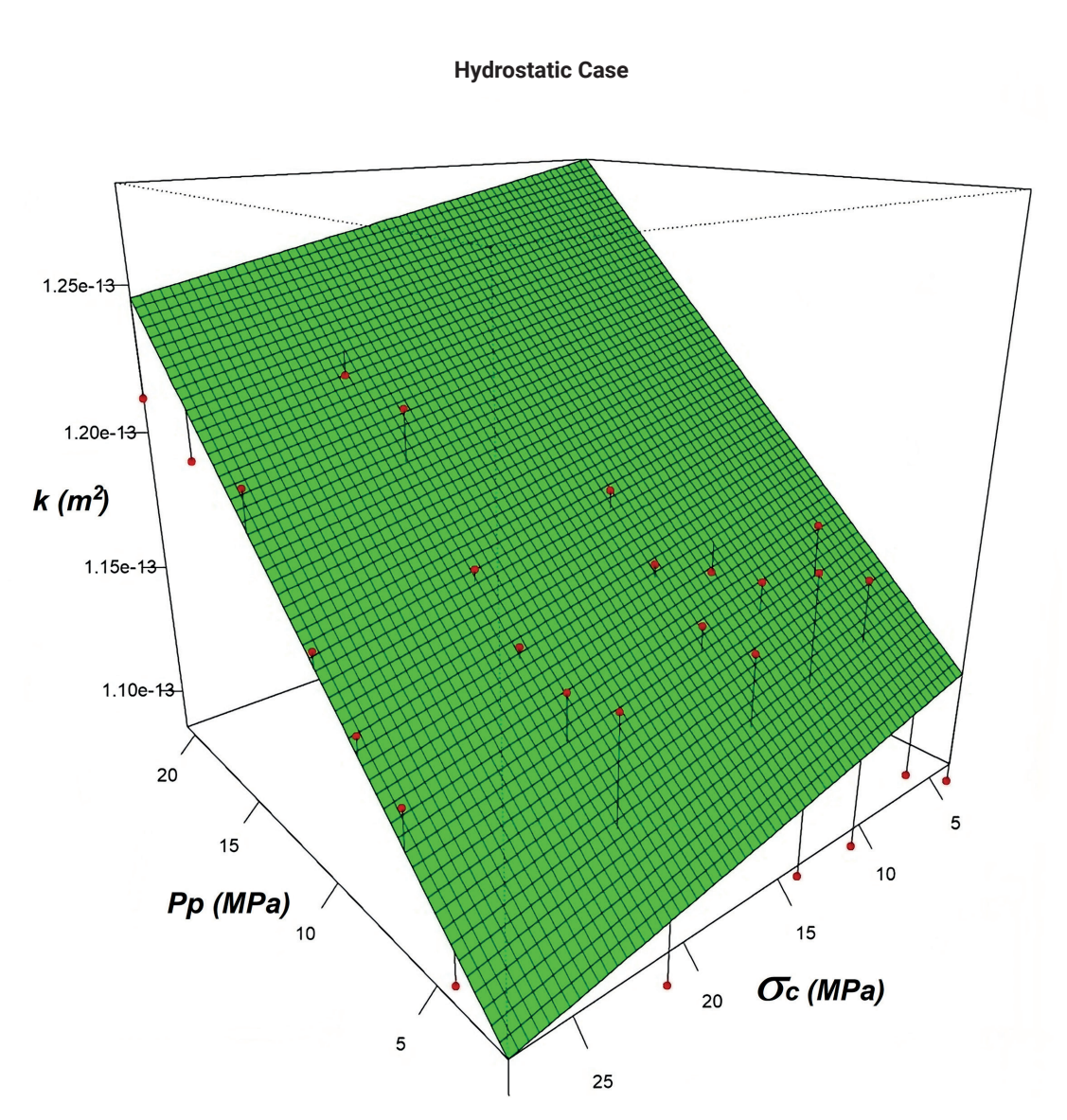


Figure 10. Permeability vs P_p and σ_c fitted by a linear model (green plane) and data points (red points) in the hydrostatic confinement mode.

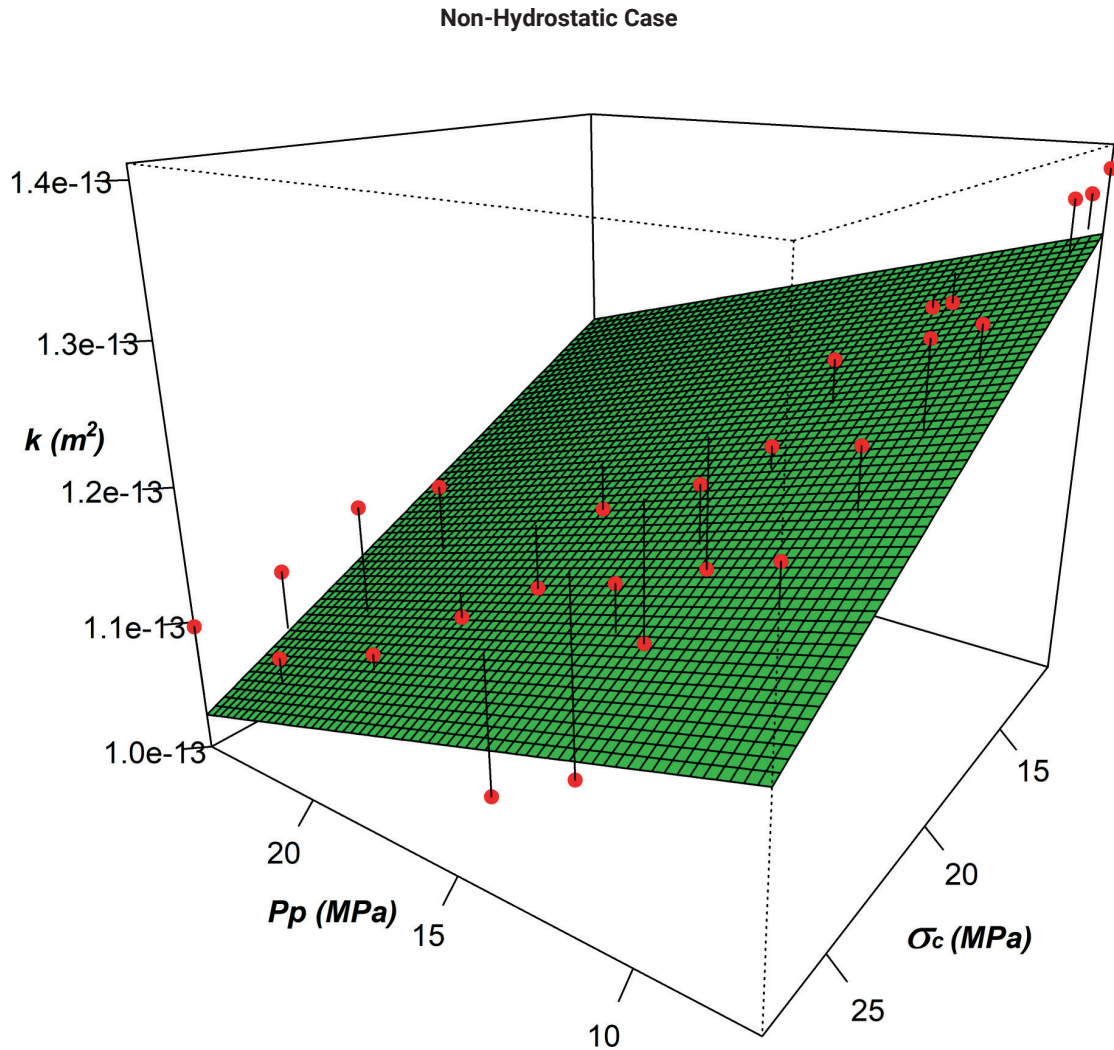


Figure 11. Permeability vs P_p and σ_c fitted by a linear model (green plane) and data points (red points) in the non-hydrostatic confinement mode.

are shown. Moreover, upon comparing Table 7 and Table 8, it becomes evident that the hydrostatic mode consistently exhibits superior data fittings in comparison to the non-hydrostatic mode.

5.2.2. Permeability data fitting in terms of effective stress σ'

Analytical fitting models frequently employed are power law, (Ghabezloo, Sulem, Guédon, & Martineau, 2009), exponential David *et al.* (1994), Nolte *et al.* (2021) and Wang *et al.* (2018) and polynomial Zhao *et al.* (2011). In this work, a linear model

$$k = B_0 + B_1 (\sigma_c - B_2 P_p), \tag{9}$$

an exponential model

$$k = B_0 e^{-B_1 (\sigma_c - B_2 P_p)}, \tag{10}$$

and a quadratic model

$$k = B_0 + B_1 (\sigma_c - B_2 P_p) + B_3 (\sigma_c - B_2 P_p)^2 \tag{11}$$

are considered. The effective stress is given by $\sigma' = \sigma_c - B_2 P_p$, where B_2 correspond to the effective stress coefficient, η_k (Bernabé, 1986). The linear and the exponential models have 3 fitting

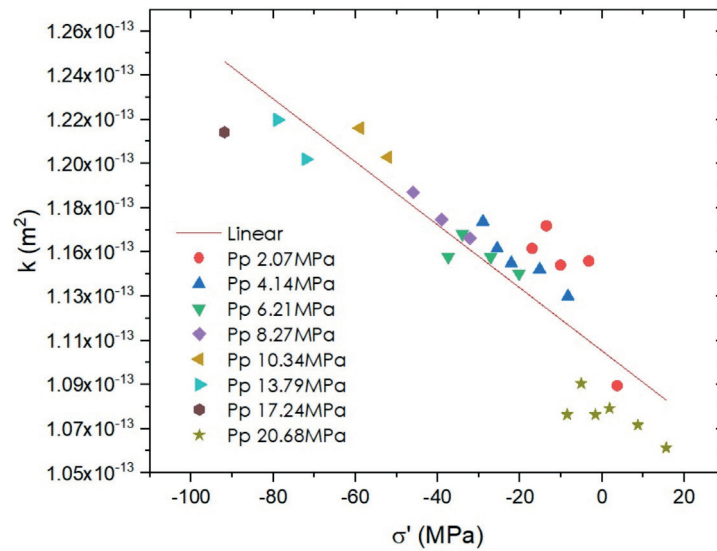


Figure 12. Permeability fitted by an effective stress linear model in the hydrostatic confinement mode.

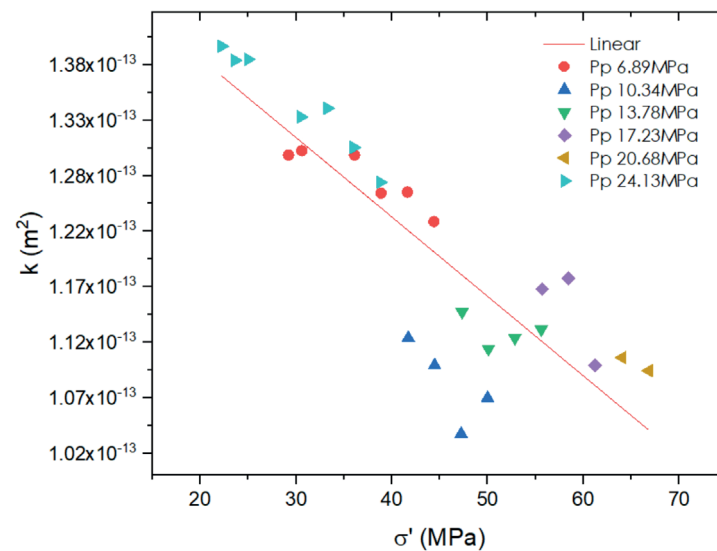


Figure 13. Permeability fitted by an effective stress linear model in the non-hydrostatic confinement mode.

parameters, and the quadratic model 4 parameters. A power law has not been considered since the effective stress in our case can attain negative values. Fitting results for the hydrostatic and non-hydrostatic mode are shown in Table 9. The linear and exponential model (both with 3 parameters) give similar fitting results. Figure 12 and Figure 13 display the linear model for permeability versus effective stress data for the hydrostatic and non-hydrostatic mode, respectively.

In the hydrostatic mode, η_k (given by B_2) is 5.78 and 5.70 for the linear and the exponential model, respectively. In the non-hydrostatic mode η_k yields -1.63 and -1.67 respectively. The

relatively large η_k value in the hydrostatic mode and the negative η_k value in the non-hydrostatic mode will be analyzed below.

5.3. Fitting results analysis and comparison with previous works

There are remarkable results obtained from the model fittings in the Bedford employed limestone samples, particularly with respect to the permeability dependence on the effective stress, which will be compared against published experiments results.

5.3.1. Dependence of permeability as function of pore and confinement stress

Results for hydrostatic confinement model in Table 7 show the expected trend, it means that permeability reduces with the confinement stress, i.e., A_1 is negative, and that permeability increases with incrementing pore pressure, A_2 positive. It is to be noticed that A_2 is around 6 times larger than A_1 . This means that fluid-carrying pore structures in the rock are much more sensitive to changes in pore pressure than to changes in confinement stress. An explanation of the phenomenon should relay on the mechanical properties and mineral composition (97% calcium carbonate) of the granular-like irregular micro-structures observed by μ CT in the Bedford limestones samples Figure 2, and their response to compression and hydrostatic stress.

On the other hand, results in Table 8 for the Bedford sample in non-hydrostatic mode display relatively less distinct impacts of pore pressure and confinement stress on permeability, since A_2 is about only 1.6 times larger than A_1 . However, a significant difference with the hydrostatic mode is that A_2 is negative, what means that permeability reduces by increasing pore pressure. This behavior has been reported by Choi *et al.* (2017) but discarded by augmenting insufficient data points or experimental errors. In this work however, there are multiple data series that seem to support the unexpected trend, even though some experimental noise is present (see Figure 9). A tentative physical explanation is that in the non-hydrostatic mode large shear stresses are present, thus pore throats become deformed and extended, in such a way that extra pore connectivity appears. When increasing the fluid pressure, the hydrostatic fluid pore pressure tends to restore throats shape, thus, reducing connectivity. This hypothesis presently lacks of experimental confirmation.

5.3.2. Dependence of permeability as function of effective stress and comparison with previous published works

The permeability dependence on effective stress is widely analyzed in diverse rock types and conditions, as described in Table 10 and Table 12, where experiments in sandstones and limestones, with various compositions, pore structure, porosity

and permeability are summarized. Also, there are cases reported in which water is employed as displacing fluid (as in this work), but also cases where gas is used instead. There is also a relatively large range of pore pressure and confinement stress explored (see Table 11), and various permeability fitting models employed, as shown in Table 12.

In this table, not a fixed model parameter value but a range of fitting parameters appear, since many authors perform permeability data fitting by data series, thus parameters are diverse. According to the reported fitting parameters in Table 12, the effective stress coefficient, η_k , covers a wide range value, but regularly, they are near or are lower than unity. Large η_k values such as 4, 7, and 16.59 are reported in sandstones by Zoback *et al.* (1975), Nur *et al.* (1980) and Zhao *et al.* (2011) respectively; and in limestones such as 3.6 and 5.0 reported by Bohnsack *et al.* (2021) Wang *et al.* (2018) respectively. These large η_k values can in some cases give place to negative effective stresses, as can be observed in Table 12. Correlations of permeability behavior with sample type or characteristics have been sought, but no relevant results are found, in part, since insufficient published data are available. Linear model fitting results obtained in this work are also reported in Table 12. The fitting η_k value for the hydrostatic confinement mode is large, it is 5.78 for the linear model and 5.70 for the exponential model. These results are consistent with the previous analysis made in Section 5.3.1, in relation to a larger permeability sensitivity to pore pressure, than to confinement stress.

5.3.3. Permeability graphical comparison with published fitting models

A graphical analysis of permeability fitting models versus effective stress for twelve well-documented published model cases displayed in Table 12, and the two linear models of this work are presented in Figure 14. From the published models, six correspond to sandstones and six to limestones. All six sandstones cases and the Han *et al.* (2022) limestone case employed gas as displacing fluid. The rest of the five limestone cases, including the cases in this paper, water was used. As described in Table 10 the six sandstone samples have similar porosity, ranging between

Table 9. Fitting parameter values for the diverse models in the hydrostatic and non-hydrostatic cases.

Parameters	Hydrostatic		Non-hydrostatic	
	Linear model	Exponential model	Linear model	Exponential model
B_0	$1.108 \times 10^{-13} m^2$	$1.109 \times 10^{-13} m^2$	$1.529 \times 10^{-13} m^2$	$1.562 \times 10^{-13} m^2$
B_1	$-1.497 \times 10^{-16} m^2 MPa^{-1}$	$-1.326 \times 10^{-13} MPa^{-1}$	$-7.294 \times 10^{-13} m^2 MPa^{-1}$	$-5.840 \times 10^{-13} MPa^{-1}$
B_2	5.78	5.70	-1.63	-1.67
$RMSE$	$2.121 \times 10^{-15} m^2$	$2.066 \times 10^{-15} m^2$	$5.520 \times 10^{-15} m^2$	$5.517 \times 10^{-15} m^2$
R^2	0.7742	0.7856	0.7290	0.7293

Table 10. Sample characteristics used in published works.

Authors	Reference	Rock type	Mineral composition	Porous framework	Porosity range (%)	Permeability (m^2)
Zoback <i>et al.</i> (1975)	(Zoback & Byerlee, 1975)	Sandstone	Clay and other various minerals	Anisotropic and rigid	20 to 24	
Nur <i>et al.</i> (1980)	(Nur, Walls, Winkler, & DeVilbiss, 1980)	Sandstone	70% to 80% quartz, 0.01% to 10% calcite, 0.14% to 2.30% dolomite, 3.97% to 8.20% amorphous silica, 2.08% to 4% feldspar and 4.32% to 20% of kaolite	Homogeneous	19	9.86×10^{-17} to 1.97×10^{-14}
Bernabé <i>et al.</i> (1986)	(Bernabé, 1986)	Sandstone		Anisotropic with cracks	6	
Bernabé <i>et al.</i> (1987)	(Bernabé, 1987)	Sandstone		Anisotropic with cracks	3	
David <i>et al.</i> (1994)	(David, Wong, Zhu, & Zhang, 1994)	Sandstone	40% to 99% quartz, 9% to 50% feldspar, 3% to 5% oxides, 3% to 5% mica, 10% to 12% clay content, clay free	Microcracks	14 to 35	4.99×10^{-12}
Warspinski <i>et al.</i> (1992)	(Warspinski & Teufel, 1992)	Sandstone	Carbonate, feldspar and litharenite	Microcracks	8 to 15	
Li <i>et al.</i> (2009)	(Li, Bernabé, Xiao, Chen, & Liu, 2009)	Sandstone	50% to 60% quartz and 30% to 40% debris	Microcracks	6.15 to 10.92	
Zhao <i>et al.</i> (2011)	(Zhao, Xiao, Li, Li, & Wang, 2011)	Sandstone	19% to 22.5% clay,	Heterogeneous	8.53 to 13.02	1.37×10^{-16} to 7.53×10^{-16}
Qiao <i>et al.</i> (2012)	(Qiao, Wong, Aguilera, & Kantzas, 2012)	Sandstone	Fine coarse litharine to quartzarenite with quartz, chert, shale and feldspar fragments	Anisotropic	5.41 to 5.87	
Li <i>et al.</i> (2014)	(Li, Xiao, Bernabé, & Zhao, 2014)	Sandstone	52% quartz, 3% feldspar, 44% lithic, 1% mica and clay particles	Granular	2.4 to 16.5	
Choi <i>et al.</i> (2017)	(Choi, Cheon, & Song, 2017)	Sandstone	81.1% quartz, 6.7% kaolite, 6.5% albite, 2.3% dolomite, 1.3% Muscovite, 2.1% biotite and carbonate	Micro-structure	16.1	
Nolte <i>et al.</i> (2021)	(Nolte, Fink, Krooss, & Litke, 2021)	Limestone	6.4% illite, 6.1% smectite, 64.4% quartz, 15.1% microcline, 8% albite	Isotropic, tight sandstone	8.57	
Feng <i>et al.</i> (2021)	(Feng, Wang, & Yang, 2021)	Limestone		Hydro-fracture	<0.6 to 8.5	9.99×10^{-19} to 1.99×10^{-16}
Selvadurai <i>et al.</i> (2008)	(Selvadurai & Glowacki, 2008)	Limestone	Calcite		17	1.59×10^{-14}
Ghabezloo <i>et al.</i> (2009)	(Ghabezloo, Sulem, Guédon, & Martineau, 2009)	Limestone	Calcite and calcite crystals	oolithic	15.7	
Da Silva <i>et al.</i> (2010)	(Da Silva, Schroeder, & Verbrugge, 2010)	Limestone	Calcite	Isotropic	27.5 to 31.8	
Wang <i>et al.</i> (2018)	(Wang, Meng, Wang, Baud, & Wong, 2018)	Limestone	78% to 100% calcite, 20% quartz and 22% dolomite	Allochemical, micritic	18 to 31	
Meng <i>et al.</i> (2019)	(Meng, Baud, Ge, & Wong, 2019)	Limestone	80% to 100% calcite and 20% quartz	Cracks and micro-fractures	14 to 16	
Bohnsack <i>et al.</i> (2021)	(Bohnsack, Potten, Freitag, Einsiedl, & Zosseder, 2021)	Limestone	Calcite, peloids/ooids, micritic	Sedimentary and diagenetic with irregular fractures	12.7 to 18.1	1.6×10^{-16} to 4.5×10^{-15}
Han <i>et al.</i> (2022)	(Han, Wu, Jiang, Fang, & Zhang, 2022)	Limestone		Simple structure		
Domínguez-Torres <i>et al.</i>	This work	Limestone	97% calcite and 3% quartz	Homogeneous	14.02	1.083×10^{-13}
Domínguez-Torres <i>et al.</i>	This work	Limestone	97% and 3% quartz	Homogeneous	13.63	1.491×10^{-13}

Table 11. Equipment and experimental conditions in published works.

Authors	Reference	Fluid	P_p range (MPa)	σ_c range (MPa)	Equipment
Zoback <i>et al.</i> (1975)	(Zoback & Byerlee, 1975)	Water	0 to 80	21 to 81.4	Triaxial cell
Nur <i>et al.</i> (1980)	(Nur, Walls, Winkler, & De Vilbiss, 1980)	Water	0.5 to 30	1 to 200	
Bernabé <i>et al.</i> (1986)	(Bernabé, 1986)	Water	10 to 30	40 to 180	
Bernabé <i>et al.</i> (1987)	(Bernabé, 1987)	Water	10 to 30	40 to 200	
David <i>et al.</i> (1994)	(David, Wong, Zhu, & Zhang, 1994)	Water	0 to 10	3 to 13	Triaxial cell
Warspinski <i>et al.</i> (1992)	(Warspinski & Teufel, 1992)	Gas	0.34 to 47	0.55 to 15	Coreholder
Li <i>et al.</i> (2009)	(Li, Bernabé, Xiao, Chen, & Liu, 2009)	Gas	0.2 to 0.8	0 to 50	Coreholder
Zhao <i>et al.</i> (2011)	(Zhao, Xiao, Li, Li, & Wang, 2011)	Gas	0 to 30	20 to 42	Coreholder
Qiao <i>et al.</i> (2012)	(Qiao, Wong, Aguilera, & Kantzas, 2012)	Gas	2 to 25	10 to 30	Coreholder
Li <i>et al.</i> (2014)	(Li, Xiao, Bernabé, & Zhao, 2014)	Gas	5 to 25	10 to 30	Coreholder
Choi <i>et al.</i> (2017)	(Choi, Cheon, & Song, 2017)	Gas	10 to 23	14 to 50	Triaxial cell
Nolte <i>et al.</i> (2021)	(Nolte, Fink, Krooss, & Littke, 2021)	Gas	10 to 30	10 to 50	Triaxial cell
Feng <i>et al.</i> (2021)	(Feng, Wang, & Yang, 2021)	Gas	1, 2 and 3	4 to 8	Triaxial cell
Selvadurai <i>et al.</i> (2008)	(Selvadurai & Glowacki, 2008)	Water	5 to 25	5 to 60	Triaxial cell
Ghabezloo <i>et al.</i> (2009)	(Ghabezloo, Sulem, Guédon, & Martineau, 2009)	Water	1.05 to 3.05	2 to 12	Triaxial cell
Da Silva <i>et al.</i> (2010)	(Da Silva, Schroeder, & Verbrugge, 2010)	Water	5	5.5 to 35.5	Triaxial cell
Wang <i>et al.</i> (2018)	(Wang, Meng, Wang, Baud, & Wong, 2018)	Water	1.2 to 5.7	3.8 to 16.4	Triaxial cell
Meng <i>et al.</i> (2019)	(Meng, Baud, Ge, & Wong, 2019)	Gas	5	5 to 85	Triaxial cell
Bohnsack <i>et al.</i> (2021)	(Bohnsack, Potten, Freitag, Einsiedl, & Zosseder, 2021)	Gas	1 to 1.5	3 to 30	Triaxial cell
Han <i>et al.</i> (2022)	(Han, Wu, Jiang, Fang, & Zhang, 2022)	Gas	0.5 to 3.5	3 to 10	Coreholder
Domínguez-Torres <i>et al.</i>	This work	Water	2.07 to 20.68	3.45 to 27.58	Hassler, Hydrostatic
Domínguez-Torres <i>et al.</i>	This work	Water	6.89 to 24.13	11.03 to 27.58	Hassler, Non-hydrostatic

Table 12. Permeability models reported in the literature.

Authors	Reference	Models ($\sigma' = \sigma_c - \eta_k P_p$)	Parameters	η_k	σ' range (MPa)
Zoback et al. (1975)	(Zoback & Byerlee, 1975)	$k = k_0 + a(bP_p - \sigma_c)$	$a = 0.014$ to 0.598 mD/bar $b = 2$ to 4	2.2 to 4	-80 to 40
Nur et al. (1980)	(Nur, Walls, Winkler, & DeVilbiss, 1980)	$k = k_0 - a\sigma_c + bP_p$	$k_0 = 0.4$ to 995 mD	0.43 to 7.1	
Bernabé et al. (1986)	(Bernabé, 1986)	$k = (A \ln \sigma_c + B)^{1/n}$	$n = 1 \times 10^{-3}$ to 9×10^{-3}	0.61 to 0.69	40 to 160
Bernabé et al. (1987)	(Bernabé, 1987)	$k = (A \ln \sigma_c + B)^{1/n}$	$n = -3.33 \times 10^{-3}$ to 0	0.4 to 0.8	41 to 160
David et al. (1994)	(David, Wong, Zhu, & Zhang, 1994)	$k = k_0 \exp(-\gamma\sigma')$	$k_0 = 14.8 \times 10^{-15}$ to 21.66×10^{-10} $\gamma = [6.62$ to $18.1] \times 10^{-3} \text{MPa}^{-1}$	0 to 0.08	0 to 300
Warspinski et al. (1992)	(Warspinski & Teufel, 1992)	$k = a_1 + a_2 \sigma_c + a_3 P_p + a_4 \sigma_c^2 + a_5 P_p \sigma_c + a_6 P_p^2$ $k = A + B \ln \sigma'$		0.65 to 0.94	35 to 70
Li et al. (2009)	(Li, Bernabé, Xiao, Chen, & Liu, 2009)	$k = a_1 + a_2 \sigma_c + a_3 P_p + a_4 \sigma_c^2 + a_5 P_p \sigma_c + a_6 P_p^2$ $k = k_0 \exp(-\gamma\sigma')$	$\gamma = [0.076, 0.097, 0.110, 0.170, 0.069] \text{MPa}^{-1}$	0 to 0.86	-175 to 25
Zhao et al. (2011)	(Zhao, Xiao, Li, Li, & Wang, 2011)	$k = a_1 + a_2 \sigma_c + a_3 P_p + a_4 \sigma_c^2 + a_5 P_p \sigma_c + a_6 P_p^2$ $k = a + b\sigma' + c\sigma'^2$		0.14 to 16.59	40 to 120
Qiao et al. (2012)	(Qiao, Wong, Aguilera, & Kantzas, 2012)			0.174 to 0.770	0 to 35
Li et al. (2014)	(Li, Xiao, Bernabé, & Zhao, 2014)	$k = a_1 + a_2 \sigma_c + a_3 P_p + a_4 \sigma_c^2 + a_5 P_p \sigma_c + a_6 P_p^2$ $k = k_0 \exp(\sigma')^{-\alpha}$	$\gamma = 6.90 \times 10^{-3}, 1.43 \times 10^{-2} \text{MPa}^{-1}$; $\alpha = 3.02 \times 10^{-1}$ and 1.83	0 to 1.5	0 to 60
Choi et al. (2017)	(Choi, Cheon, & Song, 2017)	$k = a_1 + a_2 \sigma_c + a_3 P_p + a_4 \sigma_c^2 + a_5 P_p \sigma_c + a_6 P_p^2$ $k = k_0 \exp(-\gamma\sigma')$	$\gamma = 1.08 \times 10^{-2} \text{MPa}^{-1}$; $\alpha = 1.46 \times 10^{-1}$	0 to 1.3	0 to 40
Nolte et al. (2021)	(Nolte, Fink, Krooss, & Littke, 2021)	$k = k_0 \exp(-\gamma\sigma')$	$k_0 = 10.53 \mu\text{D}$ $\gamma = 2.10 \times 10^{-2} \text{MPa}^{-1}$	1.25	0 to 40
Feng et al. (2021)	(Feng, Wang, & Yang, 2021)	$k = k_0 \exp(-\gamma(\sigma_c))$	$k_0 = 9.73, 71.88$ and 54 mD $\gamma = -8.74 \times 10^{-2}, -5.09 \times 10^{-1}$ and $-4.72 \times 10^{-1} \text{MPa}^{-1}$		
Selvadurai et al. (2008)	(Selvadurai & Glowacki, 2008)	$k = a \exp\left(-\frac{\sigma_c}{4P_0}\right)$	$P_0 = 5$ MPa		0 to 60
Ghabezloo et al. (2009)	(Ghabezloo, Sulem, Guédon, & Martineau, 2009)	$k = c(\sigma')^{-\alpha}$	$c = 0.0341 \text{mD}$ $\alpha = 0.65$	1.3	0 to 8
Da Silva et al. (2010)	(Da Silva, Schroeder, & Verbrugge, 2010)	$k = k_0 \left(\frac{\sigma'}{\sigma_0}\right)^m$		0.78 to 0.88	10 to 60
Wang et al. (2018)	(Wang, Meng, Wang, Baud, & Wong, 2018)	$k = k_0 \exp(-\gamma\sigma')$	$k_0 = 3.67 \times 10^{-13}, 1.24 \times 10^{-13}, 7.06 \times 10^{-17}$ and $3.42 \times 10^{-16} \text{m}^2$; $\gamma = 1.07 \times 10^{-3}, 1.24 \times 10^{-3}, 3.56 \times 10^{-3}$ and $3.20 \times 10^{-3} \text{GPa}^{-1}$	0.3 to 5	-8 to 16.2
Meng et al. (2019)	(Meng, Baud, Ge, & Wong, 2019)		$k = k_0 \exp(-\gamma\sigma')$	$\gamma = 2.0 \times 10^{-3}$ and $2.0 \times 10^{-2} \text{MPa}^{-1}$	0.45 to 0.95
Bohnsack et al. (2021)	(Bohnsack, Potten, Freitag, Einsiedl, & Zosseder, 2021)	$k = k_0 \exp(-\gamma\sigma')$	$k = k_0 \exp(-\gamma\sigma')$	$\gamma = 0.0087$ and 0.101MPa^{-1}	1.29 to 3.67
Han et al. (2022)	(Han, Wu, Jiang, Fang, & Zhang, 2022)	$k = a_1 + a_2 \sigma_c + a_3 P_p$ $k = a(\sigma')^\alpha$	$a = 0.385$ to $1.42 \mu\text{m}^2$ $\alpha = -4.19$ to -1.48	0.17 to 1.3	2 to 11
Domínguez-Torres et al.	This work	$k = a_1 + a_2 \sigma_c + a_3 P_p$ $k = c_1 + c_2 \sigma'$	$c_1 = a_1$; $c_2 = a_2$ $a_1 = 1.10 \times 10^{-15} \text{m}^2$ $a_2 = -1.49 \times 10^{-16} \text{m}^2 \text{MPa}^{-1}$ $a_3 = 8.650 \times 10^{-16} \text{m}^2 \text{MPa}^{-1}$ $\eta_k = -a_3/a_2$	5.78	-90 to 20
Domínguez-Torres et al.	This work	$k = a_1 + a_2 \sigma_c + a_3 P_p$ $k = c_1 + c_2 \sigma'$	$c_1 = a_1$; $c_2 = a_2$ $a_1 = 1.15 \times 10^{-15} \text{m}^2$ $a_2 = -7.29 \times 10^{-16} \text{m}^2 \text{MPa}^{-1}$ $a_3 = 1.186 \times 10^{-15} \text{m}^2 \text{MPa}^{-1}$ $\eta_k = -a_3/a_2$	-1.63	20 to 70

5% and 16% (except in the Li *et al.* 2014 case, with 2.4% porosity). The porosity of the limestone samples ranges between 13% and 16%, except the Wang cases, with larger porosity, between 19% and 31%. As shown in Table 10, the mineral composition of sandstones is mainly quartz, with a content between 50% and 81%, and other minerals as kaolite, illite, smectite or dolomite. Limestone samples are mainly calcite with some parts of quartz (also dolomite in the Wang's samples). In Figure 14a permeability in logarithmic scale as function stress is plotted. The models used are those in terms of effective stress given in Table 12. To plot each test case from Table 12, various parameter sets are involved, since many authors perform fitting using data grouping. Thus, the same model can describe different effective stress regions, but using a different parameter set (what is not adequate, as mentioned before). Anyway, the overall dependence of permeability with effective stress is plotted in Figure 14a. Most cases displayed in this figure employ exponential models, except Zhao *et al.* (2011) where a quadratic model is used, Ghabezloo *et al.* (2009), Li *et al.* (2014) and Han *et al.* (2022) where a power law model is applied, and this work, where linear models are used. Therefore, the curves in Figure 14a are straight lines except the five non-exponential models. It can be observed in this figure, that the decaying slope in many cases is very small, although some large slopes are also present. Large or small slopes do not seem to correlate with rock type (sandstone or limestone), injection fluid (water or gas), permeability value (high or low). A correlation would be expected with rock pore micro-structure and/or rock mineral composition (hard or soft mineral). However, seeking these correlations by using published literature on experimental permeability as function of stress, seems to be very difficult, since literature frequently lacks the whole required information. To further explore permeability decaying behavior in the diverse cases examined, Figure 14b has been built. Each curve in this figure has been normalized to its first (largest) permeability value, which corresponds to the lowest effective stress point of each data series. By this way, all curves start at unity and reduce with effective stress in a linear permeability scale. Since most of the models are not linear, the slope of the curve would certainly depend on the effective stress region observed. However, in the normalized permeability region near unity, slopes are exceptionally large and look very similar to each other, except the slopes of the two cases reported in this paper. This however might be a consequence of the large η_k value appearing, that makes effective stress to increase rapidly with pore pressure, giving place to small slopes. An adequate way to compare model decaying behavior would be by comparing decay rates of the exponential models. However, to do this, this model should fit all cases, which is here not the case.

6. Conclusions

A modified Hassler-type coreholder was utilized to investigate the relationship between absolute permeability and effective confinement stress in two samples of Bedford limestone. Two distinct experimental setups were utilized: the hydrostatic confinement mode, in which both the radial and axial confining stresses are equal, and the non-hydrostatic confinement mode, where core axial faces remained fixed. In both cases, distilled water at room temperature was used as displacing fluid.

For the hydrostatic case, eight experiments were conducted, applying pore pressures ranging from 2 to 20 MPa and confinement stresses ranging from 3 to 27 MPa. In the non-hydrostatic case, six experiments were performed, applying pore pressures from 6 to 24 MPa and confinement stresses from 11 to 27 MPa. Each experiment maintained a constant flow rate and the pressure drop across the core sample at various pore pressures were measured, while keeping the confinement stress constant. The experimental procedure involved cycles of different confinement stress values until all the desired values were attained. After conducting the experiments and analyzing the results, the following conclusions were drawn:

1. Statistical analysis, including bivariate analysis and Spearman correlation, reveal that in both confinement modes, hydrostatic and non-hydrostatic, there is a stronger permeability correlation to pore pressure than to confinement stress.
2. Various models were tested to fit the permeability data as a function of pore pressure and confinement stress, including bi-quadratic, bi-linear with crossing, and exponential models. For the permeability data as a function of effective stress, linear and exponential models were employed. In both confinement modes, the linear model exhibited a satisfactory fit in terms of minimal root mean square error (RMSE) and the fewest number of free parameters involved.
3. The effective stress coefficient (η_k) obtained in this study was found to be 5.78 for the hydrostatic mode and -1.63 for the non-hydrostatic mode. The hydrostatic η_k value is relatively high compared to commonly observed results, indicating that pore pressure has a stronger influence on permeability than confinement stress. The negative value observed in the non-hydrostatic mode is uncommon but has been consistently observed in the experiments. One possible explanation for this phenomenon is the alteration of the pore structure due to the presence of high shear stress in the non-hydrostatic mode. This alteration may lead to the creation of additional pore throat connections, which are subsequently restored to their original state with lower connections by increasing the pore pressure.

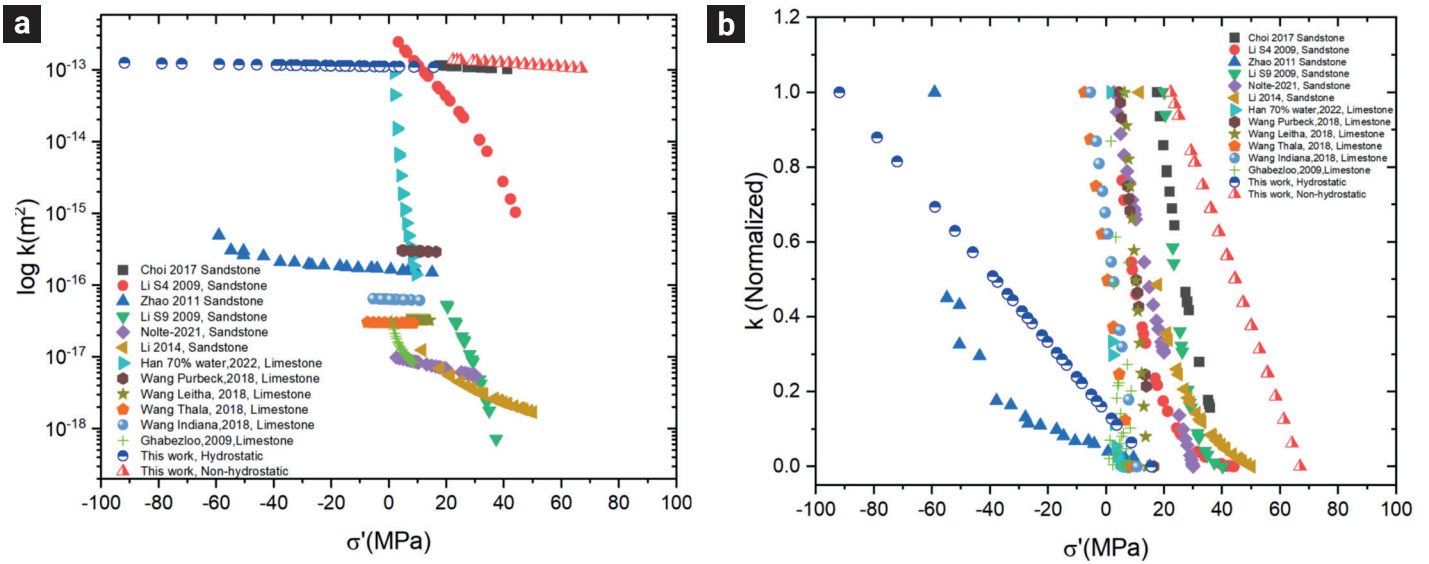


Figure 14. Permeability as a function of effective stress. In a) a logarithmic permeability scale is used, in b) a linear scale with permeability normalized to the first data point of each series.

4. The permeability results plotted as a function of effective stress, are compared and contextualized with published permeability data and fitting models in Table 10, Table 11 and Table 12, as well as Figure 14. The observed decay behavior of permeability with increasing effective stress differs from standard results, but it falls within the range of experimental observations. However, attempts to establish correlations between the effective stress coefficient (η_k), permeability decay rate, and other factors such as rock type (sandstone or limestone), displacing fluid (water or gas), permeability value, pore structure, or mineral composition were unsuccessful. This lack of correlation can be attributed to the limited availability of published information on pore structure, grain arrangement, and rock mineralogy. Therefore, the search for experimental correlations between permeability and effective stress remains an open question in this field.

7. Acknowledgements

The authors gratefully acknowledge the financial support provided by Conahcyt through the extinct Fondo Sectorial CO-NAHCYT-SENER-HIDROCARBUROS under project 280097 (2017-2024). Additionally, the author Aarón Domínguez Torres expresses his gratitude to Conahcyt for the scholarship awarded during his doctoral studies at the Mexican Petroleum Institute.

8. Nomenclature

A_n, B_n	-	Model coefficients
A	m^2	Core cross-sectional area
D	m	Core diameter
c	GPa	Compressibility
E	GPa	Young's modulus
k_{ref}	m^2	Reference permeability
K	GPa	Compressibility modulus
k	m^2	Permeability value
L	m	Core length
T	$^{\circ}K$	Temperature
P_{in}	MPa	Inlet face pressure
P_{out}	MPa	Outlet pressure
P_p	MPa	Pore pressure
Q	m^3/s	Flow rate
R^2	-	Determination coefficient
R_e	-	Reynolds number
V_r	m^3	Rock volume
W_d	kg	Core dry weight
Subscript		
0		Mean value
Greek letters		
μ	$Pa \cdot s$	Dynamic viscosity
ϕ	%	Porosity
σ_c	MPa	Confining stress
σ'	MPa	Effective stress
σ_d	MPa	Terzaghi's stress
η_k	-	Effective stress coefficient

ΔP	MPa	Pressure drop
δX		Measurement error in the variable X
Abbreviations		
BPR		Back pressure regulator
LSM		Least squares method
RMSE		Root mean square error
R^2		Determination coefficient

9. References

- Al-Wardy, W., & Zimmerman, R. W. (2004). Effective stress law for the permeability of clay-rich sandstones. *J. Geophys. Res.: Solid Earth*. 109(B4), 1-10. doi:10.1029/2003JB002836.
- Asaei, H., & Moosavi, M. (2013). Experimental measurement of compressibility coefficients of synthetic sandstone in hydrostatic conditions. *J. Geo-Eng*, 10(5), 055002. doi:10.1088/1742-2132/10/5/055002
- Bear, J. (1972). Dynamics of fluids on porous media. New York.
- Bernabé, Y. (1986). The effective pressure law for permeability in Chelmsford granite and Barre granite. *Int. J. Rock Mech. Min. Sci. and Geomech. Abstr.* 23(3), 267-275. doi:10.1016/0148-9062(86)90972-1
- Bernabé, Y. (1987). The effective pressure law for permeability during pore pressure and confining pressure cycling of several crystalline rocks. *J. Geophys. Res.: Solid Earth*. 92(B1), 649-657. doi:10.1029/JB092iB01p00649
- Bernabé, Y. (1988). Comparison of the effective pressure law for permeability and resistivity formation factor in chelmsford granite. *Pure Appl. Geophys.* 127(4), 607-625. doi:10.1007/BF00881747
- Berryman, J. G. (1992). Effective stress for transport properties of in homogeneous porous rock. *J. Geophys. Res.: Solid Earth*. 97(B12), 17409-17424. doi:10.1029/92JB01593
- Bohnsack, D., Potten, M., Freitag, S., Einsiedl, F., & Zosseder, K. (2021). Stress sensitivity of porosity and permeability under varying hydrostatic stress conditions for different carbonate rock types of the feathermalm reservoir in southern Germany. *Geothermal Energy*. 9(15), 1-59. doi: <https://doi.org/10.1186/s40517-021-00197-w>
- Choi, C. S., Cheon, D. S., & Song, J. J. (2017). Effect of pore and confining pressure on the supercritical CO₂ permeability of sandstone: implications for the effective pressure law. *Geophys. Res. J.: Solid Earth*. 122(8), 6231-6246. doi: <https://doi.org/10.1002/2017JB014475>
- Coronado, M. (2019). Technical Report Proyecto 280097. IMP (Y.61066). *Mexican Petroleum Institute*, Fondo Sectorial Conacyt-Sener-Hidrocarburos, México.
- Da Silva, M. R., Schroeder, C., & Verbrugge, J. C. (2010). Poroelastic behaviour of a water-saturated limestone. *Int. J. Rock Mech. Min. Sci.* 47(5), 797-807. doi: <https://doi.org/10.1016/j.ijrmms.2010.04.004>
- David, C., Wong, T. F., Zhu, W., & Zhang, J. (1994). Laboratory measurement of compaction-induced permeability change in porous rocks: Implications for the generation and maintenance of pore pressure excess in the crust. *Pure Appl. Geophys.* 143, 425-456. doi: <https://doi.org/10.1007/BF00874337>
- Dobrynin, V. M. (1962). Effect of overburden pressure on some properties of sandstones. *SPE Journal*. 2(04), 360-366. doi: <http://doi.org/10.2118/461-PA>
- Dong, J.-J., Hsu, J.-Y., Wu, W.-J., Shimamoto, T., Hung, J.-H., Yeh, E.-C., Sone, H. (2010). Stress-dependence of the permeability and porosity of sandstone and shale from TCDP Hole-A. *Int. J. Rock Mech. Min. Sci.* 47, 1141-1157. doi: <https://doi.org/10.1016/j.ijrmms.2010.06.019>
- Feng, K., Wang, K., & Yang, Y. (2021). Experimental study on the deformation and permeability characteristic of raw coal under the coupling effect of confining pressure and pore pressure. *Advances in Mat. Scie. Eng.* 1-8. doi: <https://doi.org/10.1155/2021/9983975>
- Ghabezloo, S., Sulem, J., Guédon, S., & F., M. (2009). Effective stress law for the permeability of a limestone. *Int. J. Rock Mech. Min. Sci.* 46(2), 297-306. doi: <https://doi.org/10.1016/j.ijrmms.2008.05.006>
- Glowacki, A., & Selvadurai, A. (2016). Stress-induced permeability changes in Indiana limestone. *Engineering Geology*. 215, 122-130. doi: <https://doi.org/10.1016/j.enggeo.2016.10.015>
- Han, J., Wu, C., Jiang, X., Fang, X., & Zhang, S. (2022). Investigation on effective stress coefficients and stress sensitivity of different water-saturated coals using the response surface method. *Fuel*. 316(123238). doi: <https://doi.org/10.1016/j.fuel.2022.123238>
- Hart, D. J., & Wang, H. F. (1995). Laboratory measurement of a complete set of poroelastic moduli for Berea sandstone and Indiana limestone. *J. Geophys. Res.: Solid Earth*. 100(B9), 17741-17751. doi: <https://doi.org/10.1029/95JB01242>
- Li, M., Bernabé, Y., Xiao, W., Chen, Z., & Liu, Z. (2009). Effective pressure law for permeability of E-bei sandstones. *J. Geophys. Res.: Solid Earth*. 114(B7), 1-13. doi: <https://doi.org/10.1029/2009JB006373>
- Li, M., Xiao, L., Bernabé, Y., & Zhao, J. (2014). Nonlinear effective pressure law for permeability. *J. Geophys. Res. Solid Earth*. 119(1), 302-318. doi: <https://doi.org/10.1002/2013JB010485>
- Lisabeth, H., & Zhu, W. (2015). Effect of temperature and pore fluid on the strength of porous limestone. *J. Geophys. Res.: Solid Earth*. 120(9), 6191-6208. doi: <https://doi.org/10.1002/2013JB01048510.1002/2015JB012152>
- McPhee, C., Redd, J., Zubizarreta, I. (2015). *Core analysis: a best practice guide*. (Vol. 64). (J. Cubitt, Ed.)
- Meng, F., Baud, P., Ge, H., & Wong, T. F. (2019). The effect of stress on limestone permeability and effective stress behavior of damaged samples. *J. Geophys. Res.: Solid Earth*. 124(1), 376-399. doi: <https://doi.org/10.1029/2018JB016526>
- Nermoen, A., Korsnes, R., Christensen, H., Trads, N., Hiorth, A., & M.V., M. (2013, June). *Measuring the biot stress coefficient and its implications on the effective stress estimate*. 47th U.S. Rock Mechanics/Geomechanics Symposium. San Francisco, California.
- Nolte, S., Fink, R., Krooss, B., & Littke, R. (2021). Simultaneous determination of the effective stress coefficients for permeability and

- volumetric strain on a tight sandstone. *J. Nat. Gas Sci. Eng.* 95(104186), 1-10. doi: <https://doi.org/10.1016/j.jngse.2021.104186>
- Nur, A. M., Walls, J. D., Winkler, K., & DeVilbiss, J. (1980). Effects of fluid saturation on waves in porous rock and relations to hydraulic permeability. *SPE J.* 20(06), 450-458. doi: <https://doi.org/10.2118/8235-PA>
- Pål Ø, A. (2022). Comparison of intercept methods for correction of state relative permeability experiments for capillary end effects. *SPE Res Eval & Eng.* 25(04), 882-899. doi: <https://doi.org/10.2118/209797-PA>
- Phillips, O. (1991). *Flow and reactions in permeable rocks*. Cambridge University Press.
- Qiao, L., Wong, R., Aguilera, R., & Kantzas, A. (2012). Determination of biot's effective-stress coefficient for permeability of nikassin sandstone. *Journal of Canadian Petroleum Technology.* 51(03), 193-197. doi: <https://doi.org/10.2118/150820-PA>
- Rose, J. (n.d.). posit.co. Retrieved from Rstudio Desktop: <https://posit.co/download/rstudio-desktop/>
- Selvadurai A. (2021). Irreversibility of soil skeletal deformations: The pedagogical limitations of terzaghi's celebrated model for soil consolidation. *Comput. Geotech.* 135, 104137. doi:10.1016/j.compge.2021.104137.
- Selvadurai, A., & Glowacki, A. (2008). Permeability hysteresis of limestone during isotropic compression. *Ground Water.* 46(1), 113-119. doi: 10.1111/j.1745-6584.2007.00390.x
- Selvadurai, A., & Glowacki, A. (2017). Stress-induced permeability alterations in an argillaceous limestone. *Rock Mech. Rock Eng.* 50, 1079-1096. doi: <https://doi.org/10.1007/s00603-016-1153-3>
- Selvadurai, A., & Selvadurai, P. (2010). Surface permeability tests: experiments and modelling for estimating effective permeability. *Proc. R Soc. Lond.* A. 466(2122), 2819-2846. doi: <https://doi.org/10.1098/rspa.2009.0475>
- Terzaghi, K. (1936). The shearing resistance of saturated soils. *Proc. 1st Int. Conf. SOil Mech*, (pp. 54-56). New York.
- Vadillo-Sáenz, M. (2022). Simulation of stress tests using a poroelastic model to estimate the permeability behavior of Bedford limestone samples. *Geofísica Internacional.* 61(3), 181-199. doi: <https://doi.org/10.22201/igeof.00167169p.2022.61.3.2129>
- Wang, Y., Meng, F., Wang, X., Baud, P., & Wong, T. F. (2018). Effective stress law for the permeability and deformation of four porous limestones. *J. Geophys. Res.: Solid Earth.* 123(6), 4707-4729. doi: <https://doi.org/10.1029/2018JB015539>
- Warspinski, N., & Teufel, L. (1992). Determination of the effective-stress law for permeability and deformation in low-permeability rocks. *SPE Form. Eval.* 7(02), 123-131. doi: <https://doi.org/10.2118/20572-PA>
- X, Z., Wu, C., & Wang, Z. (2019). Experimental study of the effective stress coefficient for coal permeability with different water saturations. *J. Pet. Sci. Eng.* 182(106282), 1-10. doi: <https://doi.org/10.1016/j.petrol.2019.106282>
- Zhao, J., Xiao, W., Li, M., Li, L., & Wang, J. (2011). The effective pressure law for permeability of clay-rich sandstones. *Petroleum Science.* 8, 194-199. doi: <https://doi.org/10.1007/s12182-011-0134-0>
- Zoback, M., & Byerlee, J. (1975). Permeability and effective stress. *Bull Am Assoc. Petr. Geol.* 59(1), 154-158. doi: <https://doi.org/10.1306/83D91C40-16C7-11D7-8645000102C1865D>

Appendix A. Permeability results analysis

The permeability experimental results have been statistically explored by box plots analysis using the open-source *R* software (Rose, s.f.). For each confining stress and pore pressure pair values, a statistical analysis of the permeability change along the time is performed once the stationary regime seems to be attained. In these box plots the mean and median permeability values and a colored box containing between 25% (*Q1*) and 75% (*Q3*) of the permeability data around the median are displayed. Also, a vertical bar for the 1.5 (*Q1*) interquartile range (from $-Q1-1.5IQR$ to $Q3+1.5IQR$), the outliers, and lines connecting the mean values and the median values respectively, are shown. In Figure 15 permeability as function of confining stress in the hydrostatic confining mode is shown for the eight different porous pressures a) to h). Green dots show outliers, while a solid black line connecting mean values, and a dashed blue line joining median values on the permeability.

In Figure 16 the corresponding permeability results for the non-hydrostatic confining mode by considering the six different pore pressures, from a) to f), are displayed.

Appendix B. Uncertainty Evaluation

The uncertainty in the permeability experimental results is evaluated by writing the variables involved in the Darcy's law as

$$\begin{aligned} \mu &\rightarrow \mu_0 + \delta\mu \\ L &\rightarrow L_0 + \delta L \\ Q &\rightarrow Q_0 + \delta Q \end{aligned}$$

$$\begin{aligned} A &\rightarrow A_0 + \delta A \\ \Delta P &\rightarrow \Delta P_0 + \delta \Delta P \end{aligned} \tag{12}$$

where subscript 0 means average value and δ values are the variation around the average. By writing the Darcy law as

$$k = \frac{(\mu_0 \pm \delta\mu)(Q_0 \pm \delta Q)(L_0 \pm \delta L)}{(A_0 \pm \delta A)(\Delta P_0 \pm \delta \Delta P)} \tag{13}$$

and defining k_0 as

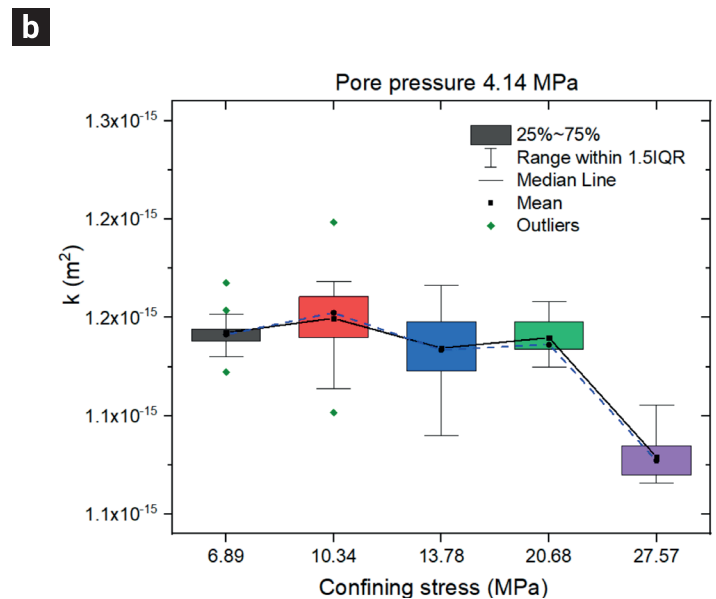
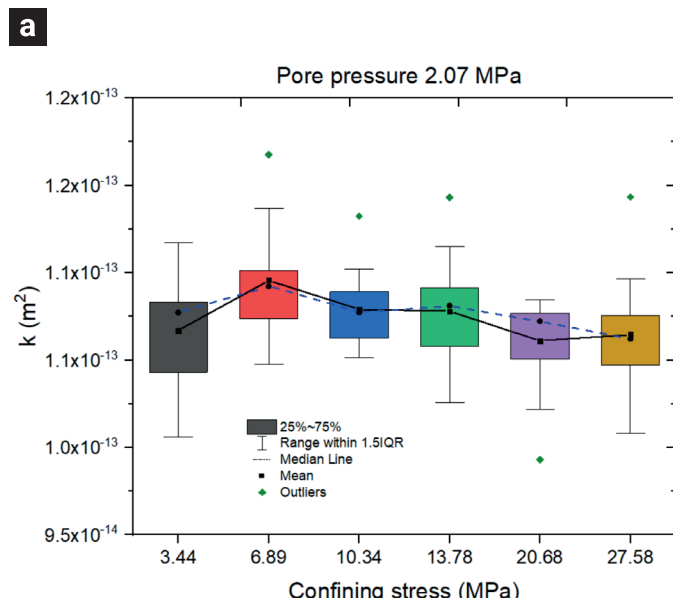
$$k_0 = \frac{Q_0 L_0 \mu_0}{A_0 \Delta P_0} \tag{14}$$

at first order we obtain the relative experimental error in permeability as

$$\frac{\delta k}{k_0} = \left[\frac{\delta\mu}{\mu_0} + \frac{\delta Q}{Q_0} + \frac{\delta L}{L_0} + \frac{\delta A}{A_0} + \frac{\delta \Delta P}{\Delta P_0} \right] \tag{15}$$

where $\delta x/x_0$ is the relative experimental error in the x variable. Further, since $A=\pi r^2$ we get

$$\frac{\delta k}{k_0} = \left[\frac{\delta\mu}{\mu_0} + \frac{\delta Q}{Q_0} + \frac{\delta L}{L_0} + 2 \frac{\delta R}{R_0} + \frac{\delta \Delta P}{\Delta P_0} \right] \tag{16}$$



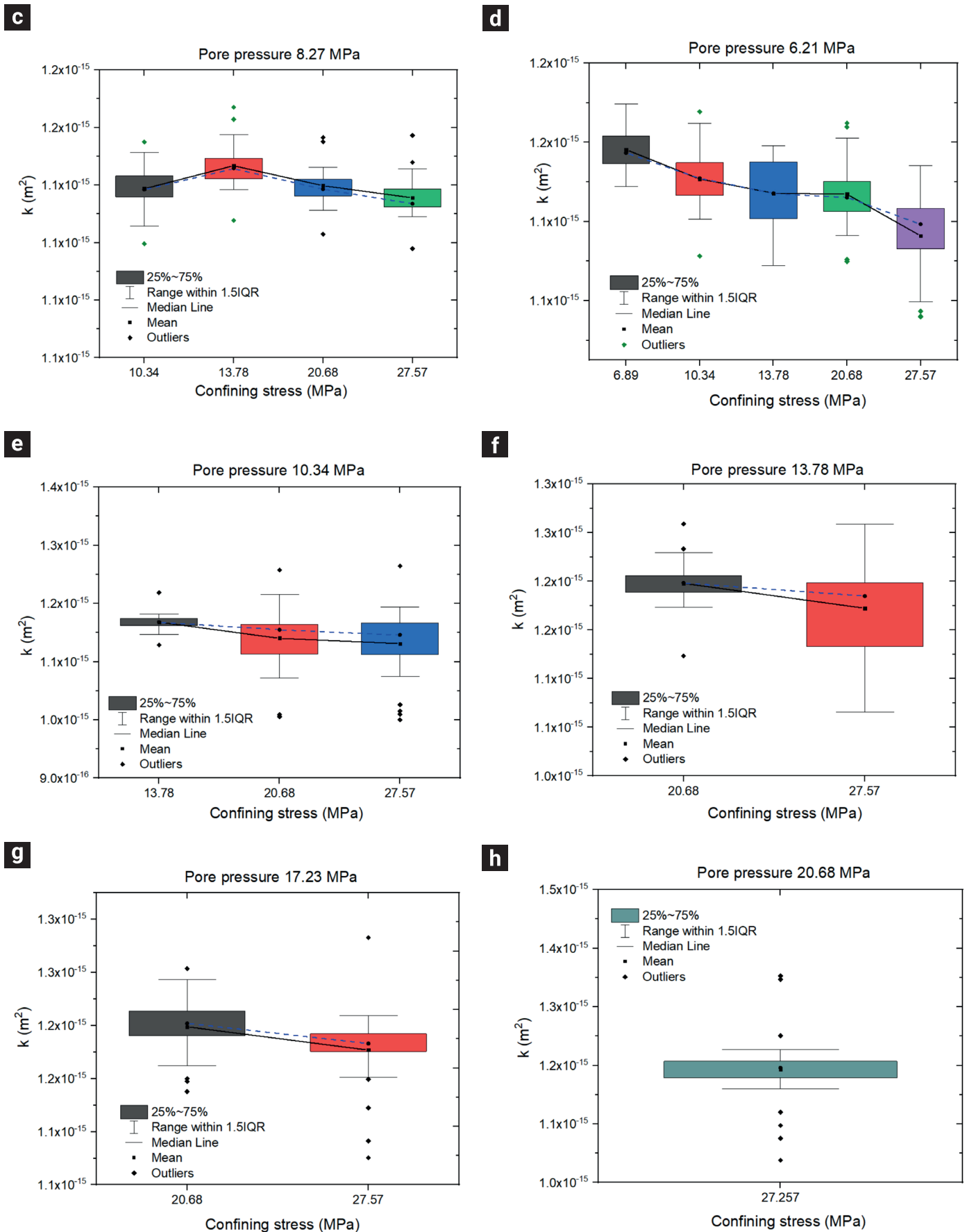


Figure 15. Permeability in the hydrostatic confining mode as function of confining stress for the eight pore pressure values employed, (a) to (h).

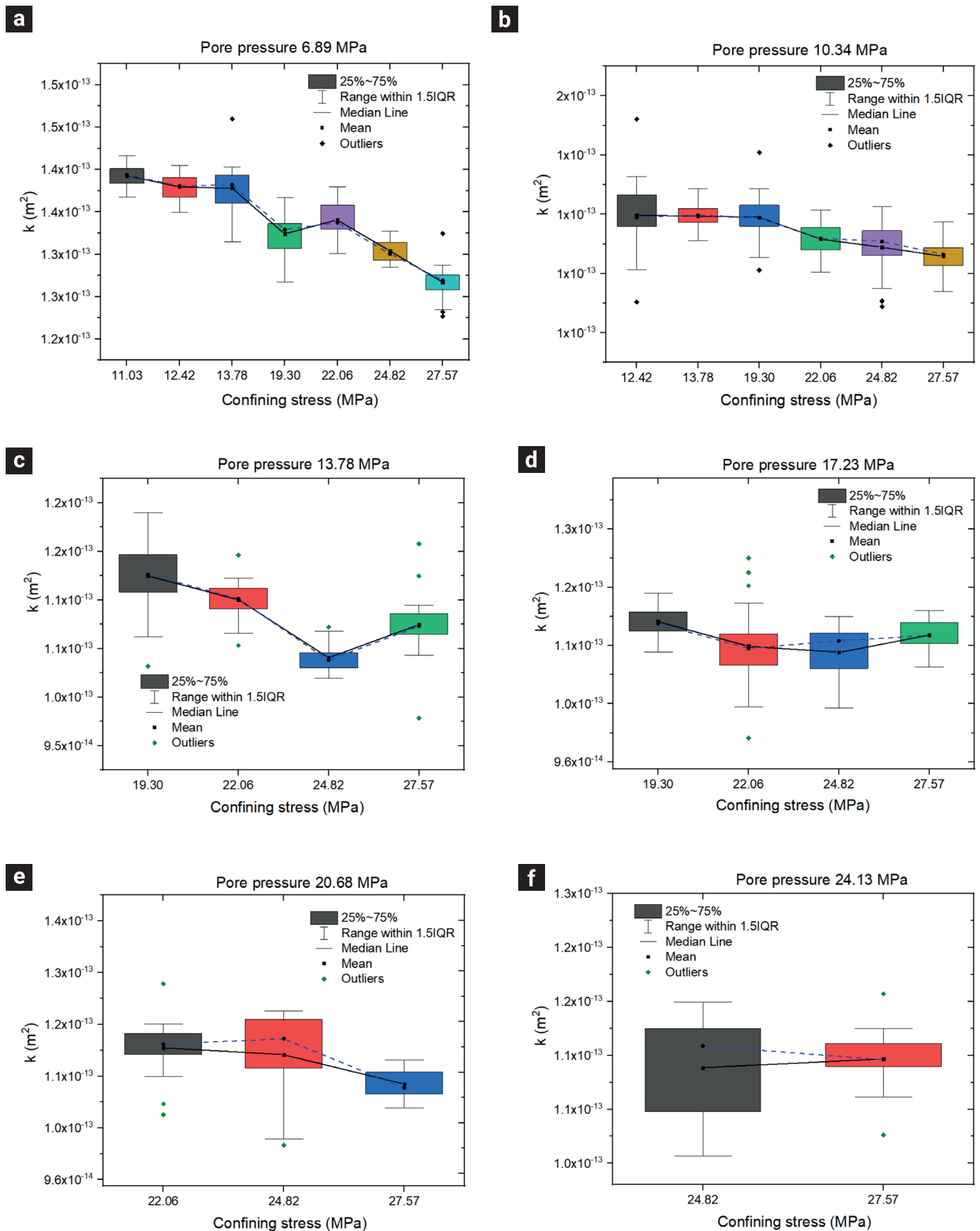


Figure 16. Permeability in the non-hydrostatic confining mode as function of confining stress for the six different pore pressure values employed, (a) to (f).